

Run-up characteristics of shoaling internal waves. February 1984.

Author: Wallace, B. C.

Publication details:

Commissioning Body: Christopher Miller Consultants Report No. UNSW Water Research Laboratory Report No. 159 0858243148 (ISBN)

Publication Date:

1984

DOI:

https://doi.org/10.4225/53/579840cbcf9e1

License:

https://creativecommons.org/licenses/by-nc-nd/3.0/au/ Link to license to see what you are allowed to do with this resource.

Downloaded from http://hdl.handle.net/1959.4/36171 in https:// unsworks.unsw.edu.au on 2024-04-20 The quality of this digital copy is an accurate reproduction of the original print copy

THE UNIVERSITY OF NEW SOUTH WALES Water research laboratory

Manly Vale N.S.W. Australia

RUN-UP CHARACTERISTICS OF SHOALING INTERNAL WAVES

bу

028-101

B.C. Wallace

Report No. 159 February, 1984



The University of New South Wales

Water Research Laboratory

RUN-UP CHARACTERISTICS OF SHOALING INTERNAL WAVES

by

B.C. Wallace

STUBSTIN OF NON SUCCESS

https://doi.org/10.4225/53/579840cbcf9e1

Report No. 159

February, 1984

BIBLIOGRAPHIC DATA SHEET	1. REPORT No. 159	2. I.S.B.N. 858243148		
3. TITLE AND SUBTITLE RUN-UP CHARACTERIS WAVES	4. REPORT DATE February, 1984			
5. AUTHOR (S)				
Brian C. Wallace 6. SPONSORING ORGANISATION	Water Research Laborato			
	Christopher Miller Cons			
7. SUPPLEMENTARY NOTES partial requirement fo	This study was undertak or the degree of Master of			
sloping bed, such as a con During the p nature have occasionally It was thought that these nal waves. Since the mech were not clearly understo with the aim of identifying	currents may be due to son hanisms responsible for gen od the investigation repor ng and quantifying these m	ed in this report. locities of a transitory mental shelf off Australia. me form of breaking inter- merating these currents ted herein was undertaken echanisms.		
ternal wave breaking and breaker height index for	run-up were developed. The	essions relating the height		
the predictive models. The wave activity on a continu	he experimental system was ental shelf in tropical to ffects the thermocline was			
with the predicted values late the observed transie	s the experimental results . Although it has not been nt velocities to the break magnitude and temporal ext	n possible to explicitly re- ing mechanisms, empirical		
	of report should be direct University of New South W	ed to the Librarian, Water ales, Manly Vale, N.S.W.2093		
10. KEY WORDS internal continental shelf - Austr	waves, shoals, density stra alia	atification, wave runup,		
	internal waves, breaker he t currents	eight index,		
12. CLASSIFICATION	13. NUMBER OF PAGES	14. PRICE		
Unrestricted	144	\$30.00		

Summary

i

This thesis examines the characteristics of internal waves shoaling upon a gently sloping bed, such as a continental shelf.

During the past decade high current velocities of a transitory nature have occasionally been recorded on the continental shelf off Australia. It was thought that these currents may be due to some form of breaking internal waves. Since the mechanisms responsible for generating these currents were not clearly understood the investigation reported here-in was undertaken with the aim of identifying and quantifying these mechanisms.

Simple predictive models which describe the basic features of internal wave breaking and run-up were developed. These models include the breaker height index for an internal wave, and expressions relating the height and celerity of the broken wave to the stage of run-up.

A series of experiments were undertaken with the aim of verifying the predictive models. The experimental system was designed to model internal wave activity on a continental shelf in tropical to sub-tropical regions. In order to minimize scale effects the thermocline was modelled by a halocline with an exaggerated density difference.

In most cases the experimental results were in good agreement with the predicted values. Although it has not been possible to explicitly relate the observed transient velocities to the breaking mechanisms, empirical relations indicating the magnitude and temporal extent of these velocities were obtained.

1.	INTRODU	JCTION	1
	1.1	General	1
	1.2	Internal Waves in Continuously Stratified Fluids	3
	1.3	Internal Waves in the Ocean	5
•	1.4	Shoaling Internal Waves	8
	1.5	The Present Study	18
2.	ANALY	SIS	20
	2.1	Introduction	2 0
	2.2	Structure	2 0
	2.3	Assumptions	24
	2.4	Shoaling of the Unbroken Wave	28
		2.4.1 Celerity of Long Internal Waves	28
		2.4.2 Parametric Description of Breaking Surface Waves	29
		2.4.3 Parametric Description of Breaking Internal Waves	32
		2.4.4 Breaker Height Index for an Internal Wave	34
	2.5	Run-Up of an Internal Wave after Breaking	40
		2.5.1 The Equation of Motion	40
		2.5.2 Order of Magnitude Analysis	42
		2.5.3 Evaluation of Similarity Solution	44
		2.5.4 Derivation of Run-up Relationships	44
3.	EXPER	RIMENTAL APPARATUS	47
	3.1	Requirements	47
	3.2	Wave Flume	47
	3.3	Mixing and Filling System	49
	3.4	Wave Generator	53
	3.5	Equipment Trolley	55
	3.6	Photographic Equipment	56
	3.7	Conductivity Probes and Meter	58
	3.8	Density Measurement	60
4.	EXPE	RIMENTAL TECHNIQUE	63
	4.1	Experimental Procedure	63
	4.2	Executing the Experiment	64
	4.3	Post-Experimental Procedure	6 8
	4.4	Optional Dye Injection	70
	4.5	Preliminary Investigations	70

5.	DATA F	EDUCTIO	N AND ANAL	LYSIS				73
	5.1	Measure	ments in t	the Constant	Depth Section	n of the 1	Flume	73
		5.1.1	Wave Heigh	nt				73
		5.1.2	Wave Celer	rity				76
	5.2	Measure	ments on t	the Sloping a	Shelf After B	reaking		78
		5.2.1	Wave Celer	rity				78
		5.2.2	Density Ex	cess Measure	ements			79
	5.3	Particl	e Velociti	ies				81
6.	EXPER	IMENTAL	RESULTS					86
	6.1	Introdu	iction					86
	6.2	Celerit	y in Const	tant Depth S	ection of the	Flume		86
	6.3	Shoalin	ig of the W	Wave on the	Sloping Shelf			87
		6.3.1	Evaluation	n of Breaker	Height Index			87
		6.3.2	Evaluation	n of Run-Up	Parameters			93
			6.3.2.1	Wave Height				93
			6.3.2.2	Wave Celerit	у			9 6
			6.3.2.3	Density Exce	ss			9 8
		6.3.3	Validity of	of the Simil	arity Solutio	n	÷	100
		6.3.4	Particle	Velocities				101
•	6.4	Scale H	Effects					105
7.	REFERE	NCES						108
	APPEND	ICES						

1 - A Summary of Experimental Data and Parameters

2 - Details of Neutrally Buoyant Particles used for Velocity Measurements

- 3 Conductivity Probes
- 4 Evaluation of $K_{\rm b}$ and ψ
- 5 List of Symbols
- 6 Application to Prototype
- 7 Papers Published by the Author Relevant to this Thesis

LIST OF FIGURES

- Streamlines and Orbits in a Progressive Internal Wave Travelling from Left to Right at the Boundary of Two Inviscid Fluids.
- The Relation between θ, the Phase and Group Velocities and the Direction of Particle Motion for Plane Waves Propagating Through a Continuously Stratified Fluid.
- 3. Oceanic Thermocline and Experimental Halocline.
- 4. Reflection Conditions at a Smooth Rigid Boundary.
- 5. Oscillatory Currents Observed at Stations PH180 and PJ140 on the Continental Shelf Off Sydney.
- 6. Schematic of Internal Wave Breaking.
- 7. The Seven Classes into which Thermal Sections from Santa Monica Bay were Grouped.
- Examples of Thermal Sections across the Continental Shelf and Adjacent Ocean Floor off Santa Monica Bay.
- 9. Schematic of Continental Shelf in Proximity of Thermocline.
- 10. Definition Sketch of a Broken Internal Wave.
- 11. Development of Surge Front.
- 12. Broken Internal Wave Propagating up a Mild Slope.
- 13. Aspect Ratio versus Run-up.
- 14. Breaker Height Index Versus Deep Water Wave Steepness for Surface Waves.
- 15. Breaking Internal Wave Type.

16. Wave Profile in Constant Depth Section of Wave Flume.

17. Idealisation of an Internal Wave at Breaking.

18. Schematic of Wave Flume.

19. Visualisation of Experiments.

20. Equipment Trolley.

21. Wave Generator.

22. Photographic Equipment.

23. Schematic of Image Recorded by Camera.

24. Conductivity Meter and Chart Recorder.

25. Thermistor Prcbe.

26. Sample Record of Raw Conductivity Probe Output.

27. Moire Screen Image Showing Wave, Scale, Timer and Chainage Markings.

28. Typical Neutrally Buoyant Particle Traces.

29. Dye and Particle Photos.

30. Definition Sketch for Wave Height Measurement in Constant Depth Section of the Flume.

31. Normalised Density Excess - Definition Sketch.

32. Measurement of Wave Celerity in the Constant Depth Section of the Flume - Conductivity Probe Output.

33. Method for Determining Celerity of Broken Wave.

- 34. Normalised Density Excess versus Elevation Above the Bed for Discrete Run-up Chainages.
- 35. Pathlines Relative to an Observer Moving with the Wave.
- 36. Wave Celerity in Constant Depth Section of the Flume.
- 37. Experimental versus Calculated Values for Breaker Height Index.
- 38. First Few Breaking Waves.
- 39. Normalised Broken Wave Height versus Run-up.
- 40. Normalised Broken Wave Celerity versus Run-up.
- 41. Normalised Density Excess versus Run-up.
- 42. Froude Number versus Run-up.
- 43. Maximum (Measured) Particle Velocities versus Distance from Breakpoint.
- 44. Sensitivity of Wave Celerity to Viscous Effects.
- 45. Conductivity Probe.
- 46. Conductivity Probe Calibration Curve.
- 47. Definition Sketch of a Gravity Current.

LIST OF TABLES

Analogies between Long Surface and Long Internal Waves
 Magnitude of the Terms in Equation (35)
 Experimental values of S_o, g_b'/g₁', F_b and K_b
 Experimental values of S_o, F, ψ and ψ/S_o
 Wave Characteristics in the Constant Depth Section of the Flume
 Wave characteristics at Breaking
 Summary of Experimental Parameters during Run-up

8. Maximum (Measured) Particle Velocities

Acknowledgements

The author would like to offer his sincere thanks and appreciation to his supervisor, Dr D. L. Wilkinson for his patience, understanding and guidance during the course of this investigation.

The interest and help received from all members of the Water Research Laboratory staff is much appreciated. In particular to Mrs C. Sherris for her diligent efforts in typing, Mrs P. Auld for meticulous drafting of the figures and Mr K. Higgs for his assistance in the production of the final manuscript. Mr J. Baird constructed the conductivity probes and the workshop staff built the wave generator and associated equipment.

Financial assistance and study leave for the author to undertake this study was provided by Christopher Miller Consultants Pty Ltd and the cooperation given by Mr C. A. Miller is gratefully acknowledged.

1. INTRODUCTION

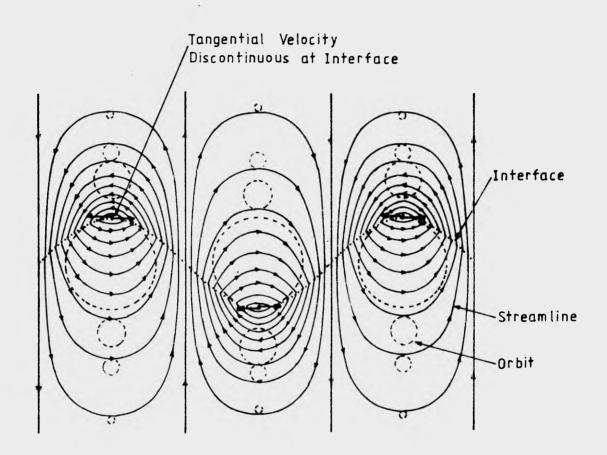
1.1 General

Large natural bodies of fluids such as the oceans are characteristically vertically stratified. In tropical to subtropical regions this is a result of solar heating of the upper layers. Due to the uniformity of salinity with depth, the density of ocean waters is primarily a function of temperature, the relatively warmer surface layers being statically stable.

When this stable stratification is disturbed internal waves can be generated. An internal wave is a periodic disturbance or wave like motion which can occur at a density interface or in a continuously stratified fluid.

An internal wave on a density interface has similar characteristics to a gravity wave on a free surface. If both layers are deep compared with the wavelength of the disturbance then the particle orbits and streamlines in a progressive internal wave (Figure 1) are analogous to those of a free surface wave. As with surface waves in deep water the internal wave energy to the first order of approximation is equally divided between potential and kinetic forms when averaged over a wavelength, and energy is propagated along the interface with a group velocity equal to half the wave celerity.

However, compared to a surface wave, the presence of the upper fluid reduces the velocity of propagation or celerity of an internal wave by a factor of $[(\rho_{\chi} - \rho_{u})/(\rho_{\chi} + \rho_{u})]^{1/2}$ where ρ_{u} and ρ_{χ} are the densities of the upper and lower layers respectively. As shown in Figure (1), the tangential velocity at the interface in an internal wave is discontinuous if the fluids are inviscid. In viscous fluids the discontinuity would



Stream	ines	and	Orb	its	in	۵	Prog	jre	ssive
Interna	Wav	e Tra	velli	ng	froi	T	Left	to	Right
at the	Boui	ndary	of	Two	o Ir	nvi	scid	Fl	uids

(After Defant, 1961)

diffuse into a vortex layer of finite thickness and diffusion would erode the interface, producing a continuous density distribution, thus modifying the flow field in the immediate vicinity of the interface.

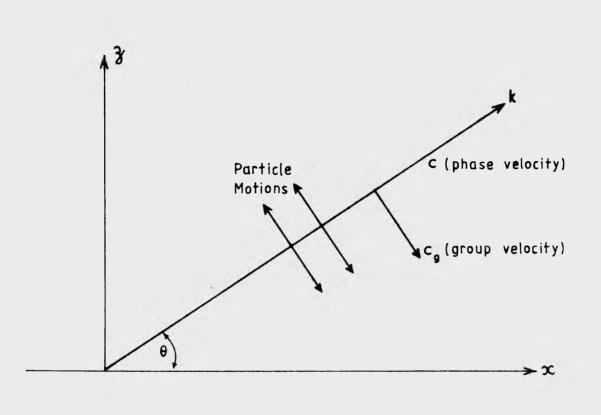
1.2 Internal Waves in Continuously Stratified Fluids

Internal wave motions in a continuously stratified medium behave differently to interfacial waves. Wave energy in continuously stratified fluids can propagate at an angle to the horizontal. Mowbray and Rarity (1967) have shown that in a continuously stratified medium the oscillatory motions produced by a small localised disturbance can be concentrated in bands bounded by rays which originate at the disturbance. Energy is transmitted along these rays which coincide with the direction of particle motions. The wave propagates at an angle (θ) to the horizontal, θ being a function of the ratio of the wave frequency (ω) and the Brunt-Väisälä frequency (N). Figure (2) shows the relationship between θ , the phase and group velocities and the direction of particle motion.

The Brunt-Väisälä or buoyancy frequency is the natural frequency of oscillation of fluid particles displaced vertically from their equilibrium position within a stably stratified fluid. The buoyancy frequency is given by:

$$N = \left(\frac{-g}{\rho} \frac{\partial \rho_0}{\partial z}\right)^{1/2}$$
(1)

where g = acceleration due to gravity ρ = density $\partial \rho_0 / \partial z$ = vertical density gradient



The Relation between θ, the Phase andGroup Velocities and the Direction ofParticle Motion for Plane Waves PropagatingThrough a Continuously Stratified Fluid

(From Turner, 1979)

The angle of wave propagation to the horizontal (θ) is given by:

$$\theta = \cos^{-1} (\omega/N)$$
 (2)

If a localised disturbance is applied to a continuously stratified fluid and ,

- if $\omega < N$, wave like motions will be generated and, for a given stratification, will propagate away from the source at an angle θ to the horizontal, or
- if $\omega = N$, the wave will propagate horizontally, or
- if $\omega > N$, the disturbance will be localised and no waves will be formed.

In a continuously stratified medium the buoyancy frequency is thus an upper frequency limit for which internal waves can exist. It should be noted, however, that sharp interfaces can sustain high frequency oscillations as the buoyancy frequency at the interface is very large in most instances.

1.3 Internal Waves in the Ocean

In tropical to subtropical regions the situation frequently arises where as a result of storm activity or the action of the trade winds, the wind stress produces a well mixed layer at the ocean surface. This stratification in the ocean which is also characterised by a sharp thermocline has been observed during the summer months along the southern California coast by Cairns and Lafond (1966) and in the Andaman Sea by Osborne and

Burch, and is similar to the vertical density distribution which has been adopted for this study (Figure 3). Note that for the experiments described here the density difference between the layers has been achieved by using a brine solution for the lower layer.

This enabled scale effects in the model to be minimised by ensuring that Reynolds numbers used in the model were as large as possible. This was achieved by exaggerating the density difference between the layers using a halocline with $(\rho_{\ell} - \rho_{u})/\overline{\rho} \sim 0.04$ to simulate the ocean thermocline where $(\rho_{\ell} - \rho_{u})/\overline{\rho} \sim 0.0004$. It will be shown in Section (6) that the Reynolds number was thereby increased by an order of magnitude.

The Reynolds number (IR), which is a measure of the ratio of the dynamic forces to the viscous forces in the flow is given by:

$$IR = \frac{cH}{v}$$
(3)

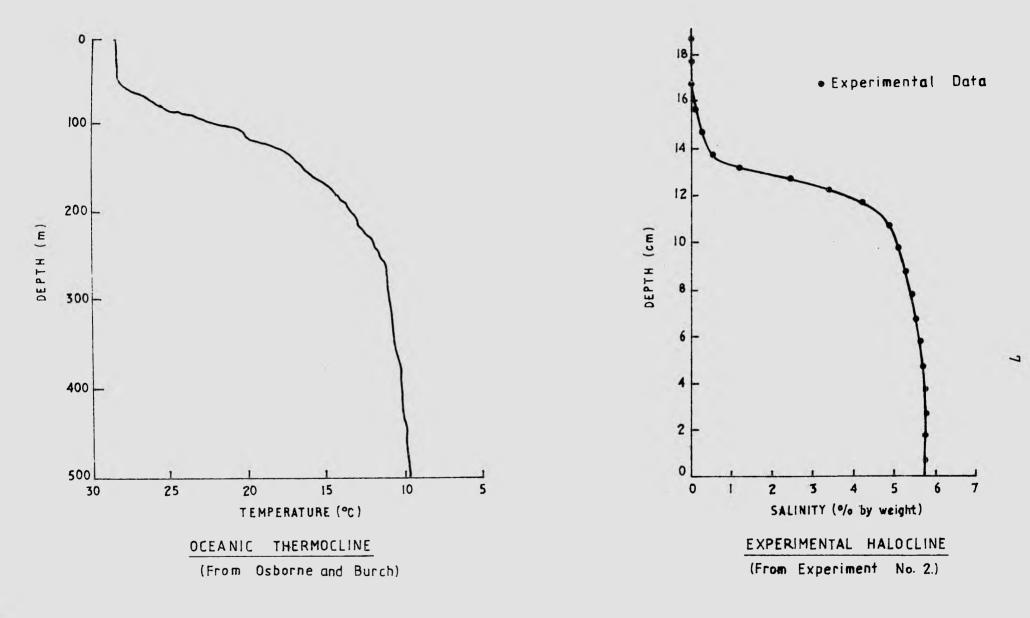
where c = wave celerity

H = wave height

and v = the kinematic viscosity.

Roberts (1975) has reported mechanisms which may be responsible for the generation of internal waves in the ocean. These mechanisms include:

- winds, air pressure fluctuations, surface swell, storms.
- generation of short period waves by long period waves, that is, the formation of internal waves of 10 to 40 min period is possibly associated with internal tides.



Oceanic Thermocline and Experimental Halocline

FIGURE 3.

- interaction between two surface waves.
- currents flowing over an irregularity on the ocean floor, such as a sill or a seamount.
- collapse of well mixed regions.

The existence of internal wave motion is seldom detectable at the ocean surface. However, the banding of the ocean surface into alternate smooth and rough bands under calm conditions has been attributed to internal wave motion.

Osborne and Burch have presented an excellent Apollo-Sayuz photograph showing surface striations at intervals of approximately 10 km and extending for distances of over 100 km in the Andaman Sea. The striations are the result of large internal waves which have modified the reflection from the sea surface. It is believed that the presence of the internal waves modulates the slopes of smaller surface waves.

Regions of the ocean where internal waves are of engineering interest are where potentially large gas or oil fields are to be found. The Oil and Gas Journal (1979) reported internal waves up to 60m in amplitude and currents of up to $\sim 1.2 \text{ m/s}$ (2.6 knots) about 110m below the sea surface in a water depth of 600m.

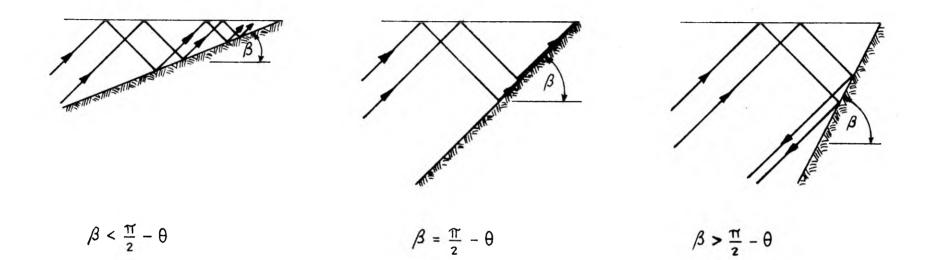
1.4 Shoaling Internal Waves

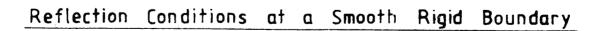
Like surface waves, the properties of internal waves are influenced by the depth of fluid in which they propagate. As first shown by Görtler (1943), internal waves in regions of continuous density gradient can be

described by ray theory, that is, the oscillatory motions are concentrated in bands bounded by rays which originate at the source of the disturbance. As the angle the rays make to the horizontal is a function of frequency only, the reflected rays must also make this angle to the horizontal, irrespective of the angle of the shelf (β). In a continuously stratified medium with constant Brunt-Väisälä frequency three possible regimes exist (Figure 4).

- If $\beta < \pi/2 \theta$, where θ is the angle of wave propagation to the horizontal as defined in Equation (2), energy will continue to propagate shoreward after reflecting from the slope, with all energy being transmitted toward the corner of the wedge formed by the boundaries. As shown in Figure (4) adjacent rays become concentrated in narrower bands indicating that the wavelength will decrease and the amplitude increase as the wave energy penetrates further shoreward.
- If $\beta = \pi/2 \theta$, the slope is critical and energy, after reflecting from the slope will propagate parallel to the slope toward the corner.
- If $\beta > \pi/2 \theta$, energy will be reflected back, parallel but in the opposite direction to the incident ray.

In practice, the concentration of energy with $\beta \leq \pi/2 - \theta$ will eventually result in the wave breaking and energy dissipation within the broken wave.

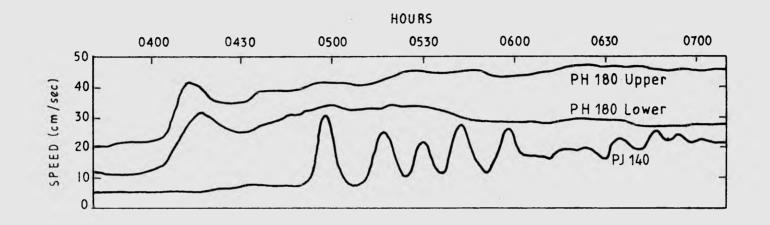


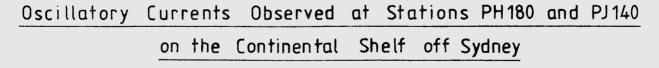


In the past decade unusually high currents have occasionally been recorded on the continental shelf off North Western Australia. These currents were transitory in nature having durations of typically less than one hour and have been observed to occur sequentially, suggesting that they might be due to groups of internal waves. However with the existing density structure the recorded velocities are too great to be attributed to orbital motions associated with simple progressive internal waves. The recorded velocities are comparable with the phase speed of the waves and for this reason it was thought that the waves might be undergoing a form of breaking where it is known there can be marked increases in the velocity of water particles.

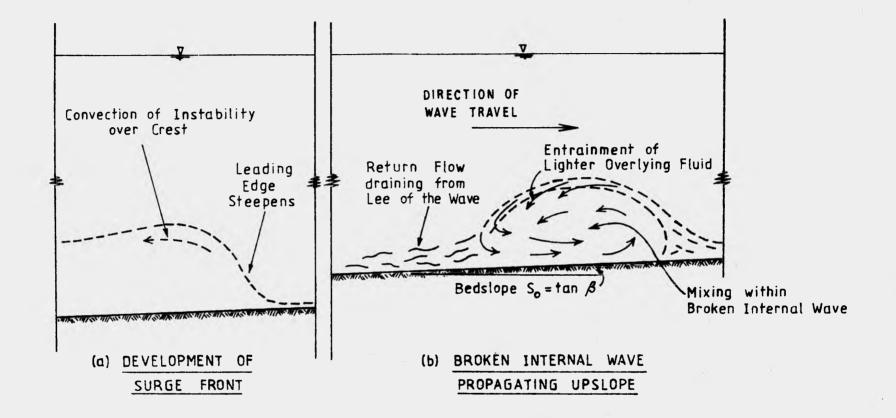
Measurements taken on the continental shelf off Sydney by Cresswell (1974) have revealed oscillatory currents of up to 0.5 m/s (Figure 5). Cresswell has shown that, for the maximum velocity to be attributed to an oscillatory internal wave, then the wave amplitude must be at least 50 m. Such an amplitude is scarcely plausible as in this instance the total depth was only 140 m and the mixed layer was only 20 m deep.

It has therefore been proposed that, internal waves, upon encountering the continental shelf will shoal and break giving rise to high particle velocities. Observations by Turner (1979), Southard and Cacchione (1972) and Murota, Hirata and Michioku (1981) show that as the sea floor approaches the thermocline, the leading edge of the wave steepens, the wave then becomes rapidly unstable, but unlike breakers on a free surface, the crests then break backwards. The breaking wave now behaves like a solitary wave. As it propagates upslope lighter overlying fluid is entrained, while mixed fluid drains from the lee of the wave, thence to form a return flow seaward. These processes are illustrated schematically in Figure (6). The analogy to surface waves is shoaling, breaking, run-up and run-down upon a





(From Cresswell, 1974)



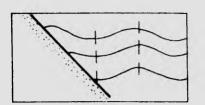
Schematic of Internal Wave Breaking

beach.

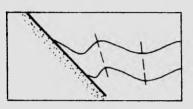
Evidence of internal swash and surf produced by internal waves was reported in the 1950's. Emery and Gunnerson (1973) have analysed bathythermogram readings from that time which show internal waves being modified on traversing the shoaling bottom of the continental shelf in Santa Monica Bay. The recorded forms were categorised into seven classes as shown in Figure (7). Class 1 shows no effects from shoaling. Classes 2,3 and 4 show forms of internal swash in which the lower isotherms reach further shoreward than would be expected from their depth above the outer shelf (in deeper water). Classes 5,6 and 7 exhibit internal surf which is characterised by temperature inversions, isolated boluses of colder water or short irregular wave forms near the bed. Thermal sections, recorded across the continental shelf in 1955-1956 which illustrate some of the above categories are given in Figure (8).

Cacchione (1970) has undertaken an experimental study of internal waves propagating over a sloping shelf in a continuously stratified medium. The slopes used, however, varied from 7° to 45° , and are much steeper than a continental shelf where slopes are typically less than 1° in the region where the thermocline approaches the bed (Figure 9). As a result of the steep slopes used in Cacchione's experiments, the processes which he observed may be appreciably modified on a (much shallower) continental shelf.

Exploratory experiments undertaken by Southard and Cacchione (1972) in a two layer medium have shown a similar pattern of breaking to that observed by the author, that is, a backwards breaking wave forming a turbulent vortex propagating upslope with a compensating return flow of mixed fluid. The slope, however, used by Southard and Cacchione was 0.1, much



1. INTERNAL WAVES WITH NO EFFECT BY SHOALING BOTTOM: ISOTHERMS SIMILAR AT DIFFERENT DEPTHS



3. INTERNAL SWASH: SHALLOWER ISOTHERMS PRECEDE DEEPER ONES: MARKED STEEPENING OF WAVE FRONT



5. INTERNAL SURF: TEMPERATURE INVERSION



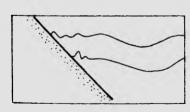
2. INTERNAL WAVES WITH NO EFFECT BY SHOALING BOTTOM: WAVE PATTERN SUPERIMPOSED ON GENERAL TEMPERATURE SLOPE DUE TO UPWELLING



4. STRONG INTERNAL SWASH : DEFINITE WAVE RUN-UP



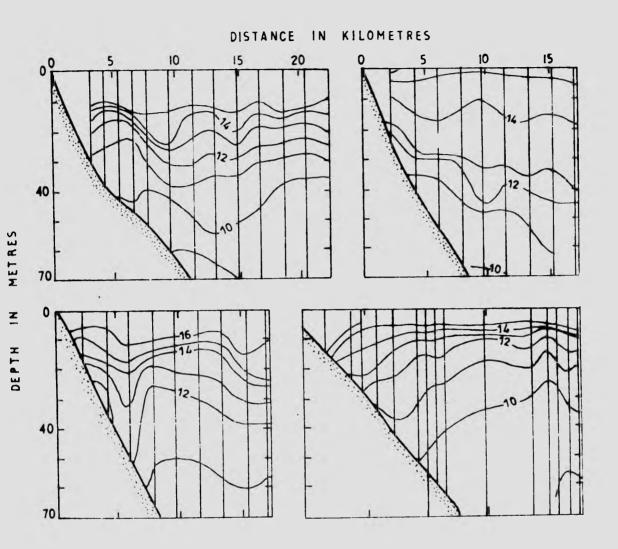
6. INTERNAL SURF: DISCRETE BOLUS OF COLD WATER ALONG THE BOTTOM



7. INTERNAL SURF: EXTREME IRREGULARITY IN WAVE FORM NEAR THE BOTTOM

The Seven Classes into which Thermal Sections from Santa Monica Bay were Grouped (From Emery and Gunnerson, 1973)

FIGURE 7.

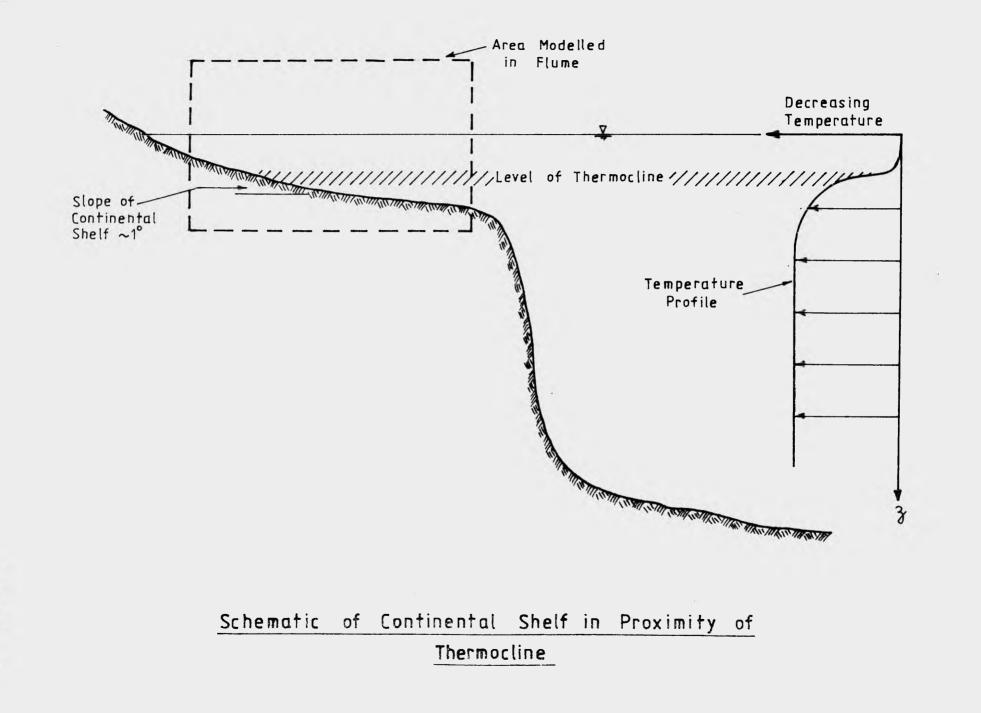


NOTE :

These sections made by bathythermograph lowerings during 1955-1956, illustrate classes 3,4,6 and 7 of internal swash and surf, as defined in Figure (7)

Examples of Thermal Sections across the Continental Shelf and Adjacent Ocean Floor off Santa Monica Bay (From Emery and Gunnerson, 1973)

FIGURE 8



steeper than the slopes used by the author. This may account for their observation of an abrupt break at a position well downslope of the original level of the interface and subsequent rapid dissipation of the breaker vortex, whereas the author observed a gradual break, approximately at the original level of the interface and a somewhat slower dissipation of the breaker vortex.

Hall and Pao (1969) have conducted experiments on the breaking of internal waves on a slope of about 0.1. Their experiments were undertaken in a small wave tank $(2.9 \text{ m} \times 0.5 \text{ m} \times 0.4 \text{ m})$ with an immiscible, two-layer system. The waves were observed to amplify slightly, steepen asymmetrically and then break in a violent process of overturning with random small scale motion. Although this is comparable to the initial break as observed by the author, as Hall and Pao conducted their experiments with immiscible fluids, entrainment, mixing and the production of the return flow may not have been modelled correctly.

More recently Murota, Hirata and Michioku (1981) have undertaken experiments in a miscible two layer system with shelf slopes of 0.05 and 0.10. The paper, however, is very brief, consisting predominately of a qualitative description of the actual breaking process only, which is in agreement with the observations of Turner (1979) and Southard and Cacchione (1972) as previously described.

1.5 The Present Study

The purpose of the research undertaken in this study was:

- To provide an experimental system that would as nearly as practical reproduce the shoaling and breaking processes as would occur when an oceanic internal wave propagates over a continental shelf.
- To relate those processes to unexplained transient currents which have previously been recorded on continental shelves in various locations.
- To develop a simple predictive model to describe the basic features of internal wave run-up.

The experimental system was designed to model internal wave activity on a continental shelf in tropical to subtropical regions where a strong thermocline is usually found between 30 m and 150 m depth.

As noted earlier the density distribution was modelled by a layer of fresh water overlying a layer of saline solution, the depth of the halocline being small compared to the particle orbits. The depth of the upper layer was sufficient to ensure that surface waves were negligibly small. Later experiments conducted with a diffuse halocline (compared with the scale of the particle orbits) showed a similar pattern of internal wave shoaling and breaking to that with a sharp interface.

2. ANALYSIS

2.1 Introduction

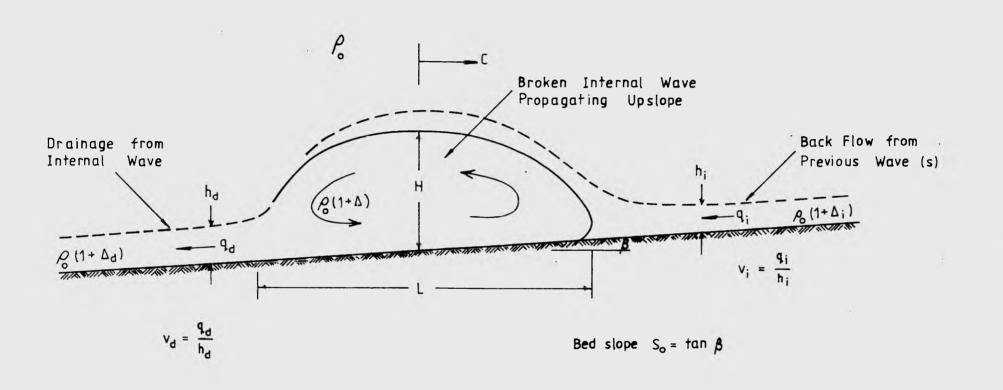
In this chapter we examine:

- The structure of an internal wave at breaking and of a broken internal wave propagating up a gently sloping shelf, and
- A theory relating the parameters which describe an internal wave at breaking to the parameters which describe a (non-broken) internal wave propagating in a fluid of constant depth, and
- A theory which describes the characteristics of internal wave run-up on a gently sloping shelf after breaking.

2.2 Structure

An idealization of the flow pattern which describes an internal wave from breaking to the limit of run-up is shown in Figure (10). The parameters describing the flow are summarised as follows:

A broken internal wave of height (H), length (L) and density $\rho_0(1 + \Delta)$ is propagating upslope with celerity (c) through an ambient fluid of density (ρ_0). The backflow (q_1) from the previous wave(s) is of depth (h_1) immediately upslope of the present wave and density $\rho_0(1 + \Delta_1)$. The density and depth of the backflow (q_d) from the present wave are $\rho_0(1 + \Delta_d)$ and (h_d) respectively. The bedslope is S_0 .



2

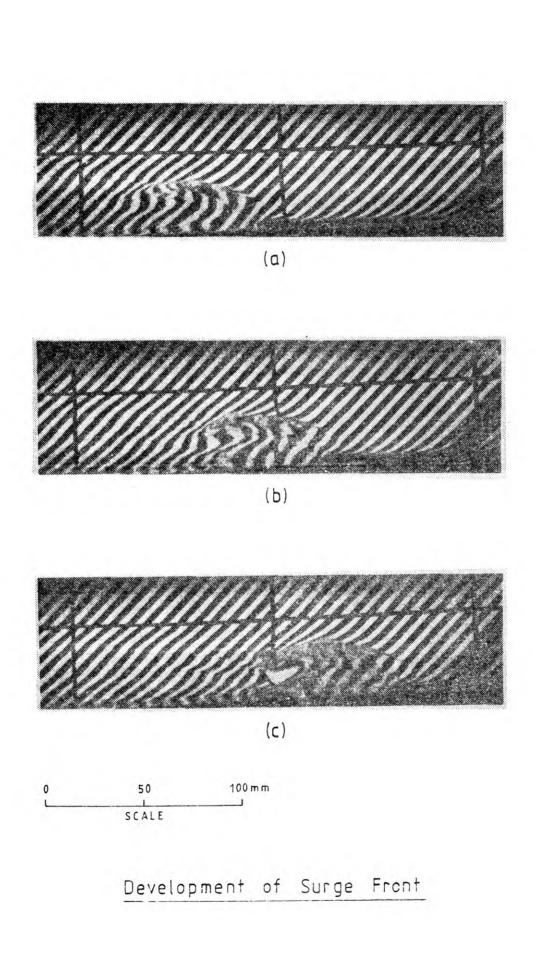
Definition Sketch of a Broken Internal Wave

Figure (11) shows Moiré screen images of an internal wave breaking on a gently sloping shelf. The time interval between photographs is 0.5 seconds and the location of the Moiré screen (and chainage lines) is the same in each photograph. The development of the surge front and transformation to a solitary wave form is shown in the sequence of photographs in Figure (11).

Figure (11a) shows the initial stage of transformation. The wave is travelling from left to right and the wave face has undergone considerable steepening giving the wave a surge like appearance. There is a marked change to the intensity of the vertical density stratification on the leading edge or landward side compared to the leeward or ocean side. The wave shows clear signs of instability on the forward face as evidenced by the irregular distortion of the Moiré screen.

Figure (11b) taken moments later shows the region of instability being convected over the crest. The geometry continues to change rapidly and in Figure (11c) the region of instability has now been convected back over the crest. An intense roller is developing on the leeward face of the wave, the direction of circulation being anti-clockwise as viewed in the photograph.

Tracking of neutrally buoyant particles revealed that very high velocities are achieved within the roller, of up to 50% greater than the wave celerity in regions near the bed. Exploration with dye probes revealed considerable entrainment of lighter fluid from above into the roller as it forms.



FIGURE

The structure and celerity of the internal wave after transformation are similar to that of a solitary wave. The structure of the solitary wave form propagating upslope is shown in the sequence of photographs in Figure (12). In Figure (12a) fine scale turbulence has developed throughout the roller region as evidenced by the complete obliteration of the Moiré screen while the forward face of the wave remains streamlined.

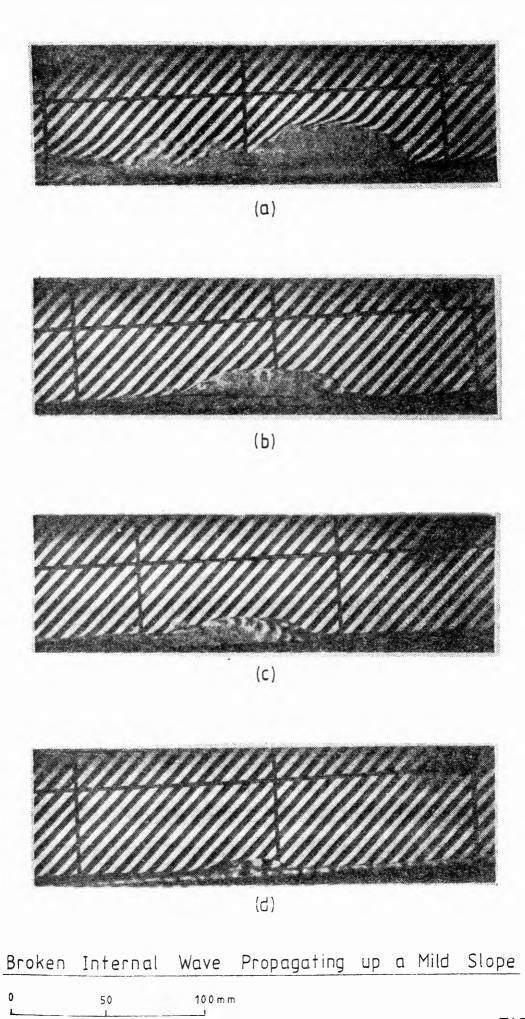
Figure (12b) shows the wave at time 0.2 of a period later and the wave form has stabilised and remains basically unchanged during the remainder of the run-up. The forward face of the wave is smooth and streamlined while the rearward face is turbulent and broken. The turbulence decays rapidly behind the wave, assisted by the stabilizing effect of the strong vertical density gradient.

Figure (12c) shows the turbulence within the roller decaying as the Moiré screen again becomes discernible through the wave. Maximum particle velocities are now approximating the wave celerity.

The wave is nearing the limit of run-up in Figure (12d) and will completely dissipate within this frame.

2.3 Assumptions

The analysis to be presented attempts to describe the variation in the characteristic properties of an internal wave at breaking and the subsequent run-up. The computations are much simplified if the following assumptions are adopted.



	50	100 m m
····		
	SCALE	

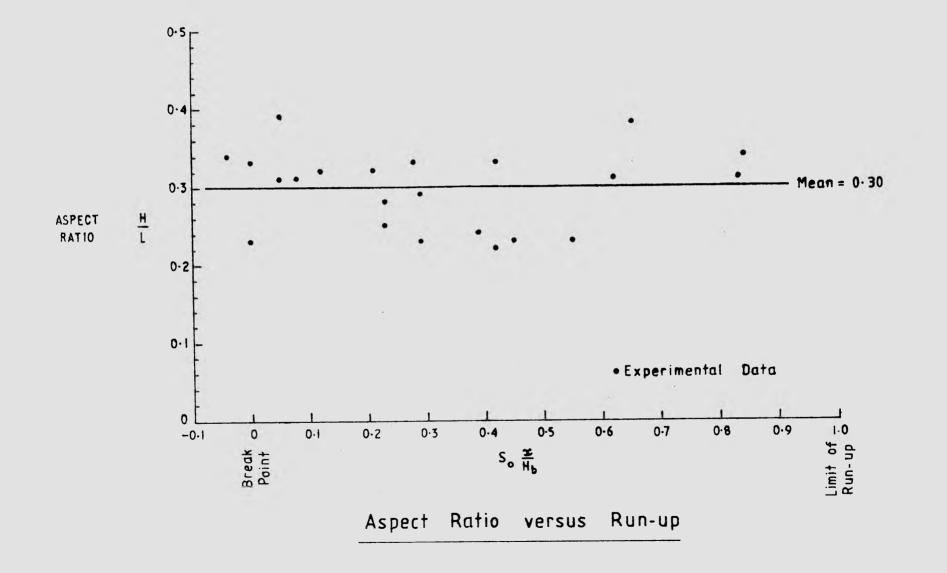
FIGURE • As the differences in density between the two fluids are small one may adopt the Boussinesq approximation which consists essentially of neglecting variations in density in so far as they effect inertia, but retaining them in the buoyancy terms. Mathematically this may be expressed as:

$$\rho = \rho_0 (1 + \Delta) \simeq \rho_0 \tag{4}$$

and

• The form and density structure of the broken wave is self preserving. Experiments to be described in Section (6) have shown that the structure of internal waves after breaking is very nearly self similar, that is, the aspect ratio, defined as H/L remains constant thoroughout the run-up. This approximation is quite reasonable as can be seen from Figure (13) which shows a plot of aspect ratio versus run-up. The aspect ratio shows no dependence on stage of run-up and is fairly uniformly distributed about a mean value of 0.3. The sectional area of a 2dimensional wave (A) can therefore be expressed as:

 $A = S_1 H^2$ (6) where $S_1 = a$ dimensionless shape factor.





2.4 Shoaling of the Unbroken Wave

2.4.1 Celerity of Long Internal Waves

The dispersion relation for a progressive internal wave propagating between layers of finite thickness is given by Lamb (1952) as:

$$c^{2} = \frac{g(\rho_{\ell} - \rho_{u})}{k} \quad (\rho_{u} \operatorname{coth} kd_{u} + \rho_{\ell} \operatorname{coth} kd_{\ell})^{-1}$$
(7)

where d_u , d_{λ} = the depths of the upper and lower layers respectively,

 $k = 2\pi/\lambda_o$,

and λ_0 = the deepwater wavelength.

Where $\lambda_0 >> d_u$, d_k we can write with sufficient accuracy:

$$\begin{array}{l} \operatorname{coth} kd_{u} &\simeq 1/kd_{u} \\ \operatorname{coth} kd_{k} &\simeq 1/kd_{k} \end{array} \tag{8}$$

Substituting Equations (8) and (9) into Equation (7) and simplifying yields:

$$c_{1}^{2} = \frac{g(\rho_{\ell} - \rho_{u})}{\rho_{u}} \cdot \frac{d_{u} d_{\ell}}{(d_{u} + d_{\ell})}$$
(10)

In terms of the effective gravitational acceleration $[g_1' = g(\rho_{\chi} - \rho_u)/\rho_u]$ Equation (10) becomes:

$$c_{1} = \left[\frac{g_{1}' d_{u} d_{\lambda}}{d_{u} + d_{\lambda}}\right]^{1/2}$$
(11)

Equation (11) gives the celerity (c_1) of an internal wave confined between horizontal upper and lower boundaries where the wavelength is much greater than the distance between the boundaries. The celerity of an equivalent long surface wave as described by linear theory is:

$$c = (gd)^{1/2}$$
 (12)

where d = the depth of water in which the wave propagates.

The analogies between long surface and long internal waves are summarised in Table 1.

TABLE 1. Analogies Between Long Surface and Long Internal wav	TABLE I.	Analogies	Between	Long	Surface	and	Long	Incernal	wave
---	----------	-----------	---------	------	---------	-----	------	----------	------

	Surface Wave	Internal Wave
Effective Gravitational Acceleration	g	$g' = \Delta g$ $d_{1}d_{2}$
Equivalent Fluid Depth	d	$D = \frac{d \chi}{d_u + d_{\ell}}$
Celerity	(gd) ^{1/2}	(g'D) ^{1/2}

2.4.2 Parametric Description of Breaking Surface Waves

In the previous section the analogous parameters describing surface waves and internal waves were introduced. This process will now be extended to cover the analogous parameters describing the breaking characteristics of surface and internal waves. Munk (1949) derived an expression for the breaker height index H_b/H'_o for surface waves of the form:

(13)

$$\frac{H_{b}}{H_{o}} = \frac{1}{3.3(H_{o}'/\lambda_{o})^{1/3}}$$

where H_b = wave height at breaking, H_o' = unrefracted deepwater wave height, and λ_o = deepwater wavelength

Subsequent investigations have established that H_b/H_o' depends not only upon the incident wave steepness (H_o'/λ_o) , but also on the beach slope (S_o) .

Goda (1970) derived empirical relationships (for surface waves) between H_b/H_0' and H_0'/λ_0 for several beach slopes. A plot of these relationships as shown in Figure (14) reveals that a steeper beach slope (S₀) produces a greater breaker height index (H_b/H_0') for a given deepwater wave steepness, and an increased deepwater wave steepness produces a lower breaker height index for a given bedslope.

Surface breaking waves have also been classified into spilling, plunging, or surging depending on the way in which they break. Patrick and Weigel (1955) have made a general division between the different types of break as follows:

> Spilling breakers occur when steep deepwater waves shoal onto mildly sloping beaches.

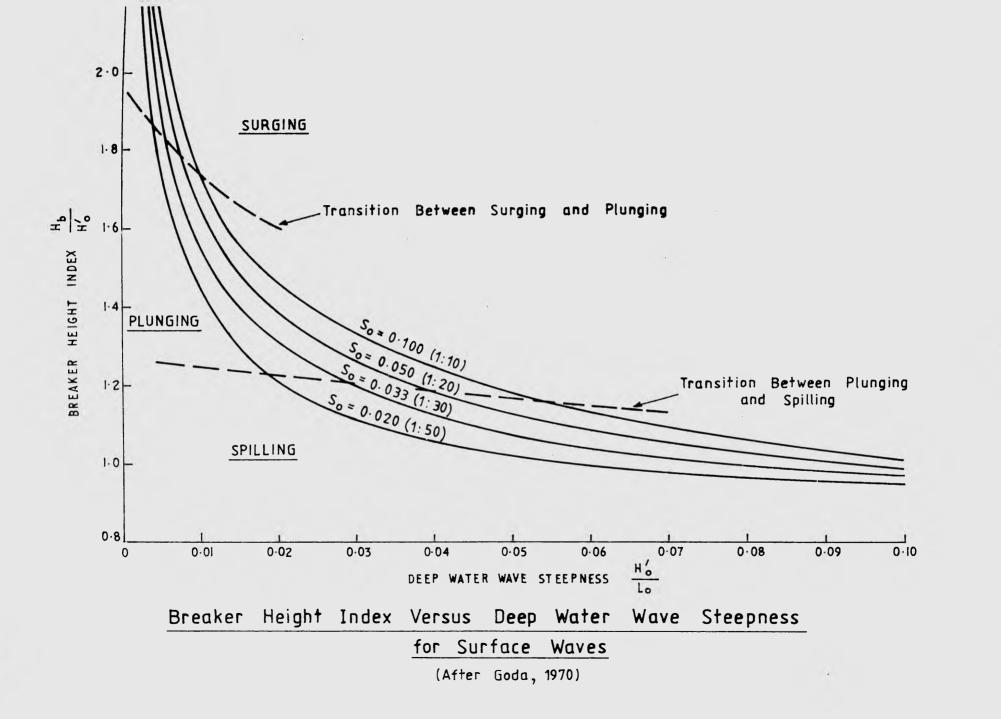


FIGURE 14.

щ

- Plunging breakers form when waves of intermediate steepness shoal onto steeper beaches.
- Surging breakers are associated with flat deepwater waves shoaling onto steep beaches.

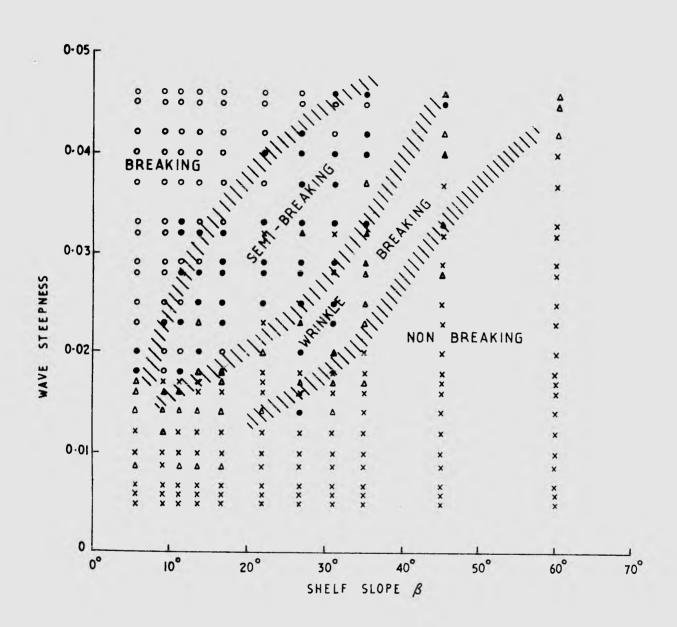
2.4.3 Parametric Description of Breaking Internal Waves

If the analogy between surface and internal waves can be extended to the breaking process, then we would expect that internal wave characteristics at breaking are also a function of the bedslope, and the wave slope prior to breaking.

An examination of the literature describing breaking internal waves has revealed only one author (Nagashima, 1971) who has examined and categorised breaking internal waves with respect to the slope of the shelf at breaking and the wave steepness prior to breaking. Nagashima has divided breaking internal waves into breaking, semi-breaking, wrinklegenerating and non-breaking categories. However, as shown in Figure (15), the range of bedslopes used were from the vertical down to a slope of 0.06 $(\sim 3.5^{\circ})$ which is still very much steeper than those in the present study.

In model studies using flatter bedslopes $(<5^{\circ})$ which were undertaken by, amongst others, Murota et al (1981) there were no appreciable differences in the breaking mechanism to that observed in experiments to be described in Section (6).

In the following section an expression analogous to Equation (13) will be derived for the breaker height index of an internal wave.



LEGEND:

- Breaking waves which in the process of breaking generate much foam
- <u>Semi-breaking</u>-waves appear to break but do not generate stable foam
- <u>Wrinkle generating</u>- waves in which there is no gross deformation, but short capillary waves are generated
- * Non breaking waves in which there is no noticeable deformation.

Breaking Internal Wave Type

(After Nagashima, 1971)

FIGURE 15.

2.4.4 Breaker Height Index for an Internal Wave

The derivation of the breaker height index for internal waves is based on the following assumptions:

- The wave profile in the constant depth region of the flume can be described by linear wave theory. Examination of Figure (16) shows that the variation of the elevation of the halocline with time can be reasonably approximated by a sine curve.
- Energy is conserved up to the time of breaking and the group velocity is equal to the phase speed of the wave.

Linear theory gives the energy of a single 2-dimensional wave E, as:

$$E_{1} = \rho g_{1}' H_{1}^{2} \lambda_{1} / 8 \tag{14}$$

where H_1 = the wave height in the constant depth section of the flume, λ_1 = the wavelength in the constant depth section of the flume, and $g_1' = \Delta_1 g$

in which Δ_1 = the density excess within the lower layer in the constant depth section of the flume.

 $= (\rho_{g} - \rho_{11})/\overline{\rho}$

In experiments it was difficult to define an actual point of breaking. The initial break was observed to occur over finite a distance of $\sim 3H_b$ as was shown in Figure (11). However, the breaking region was located approximately at the intersection of the mean level of the halocline (with no wave activity) and the bed as shown schematically in Figure (17).

INCREASING CONDUCTIVITY

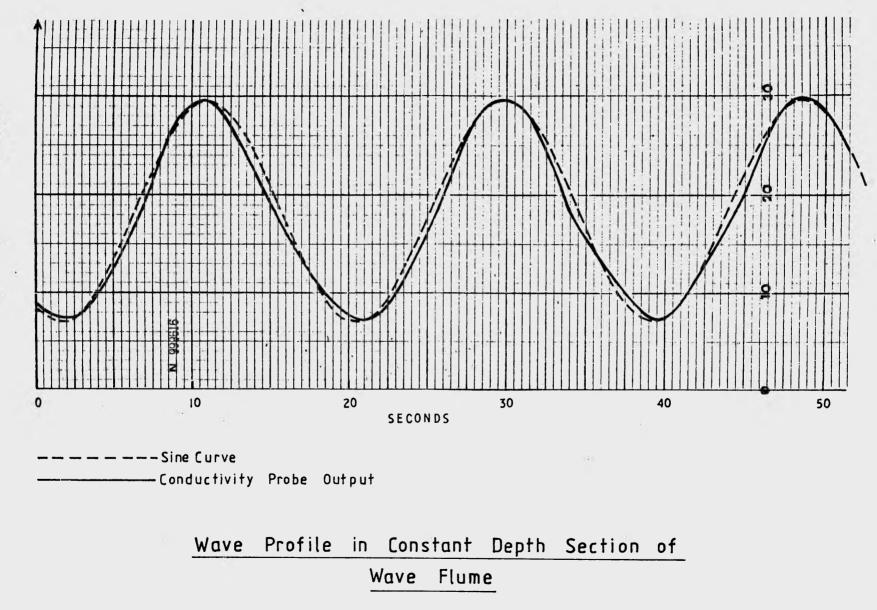
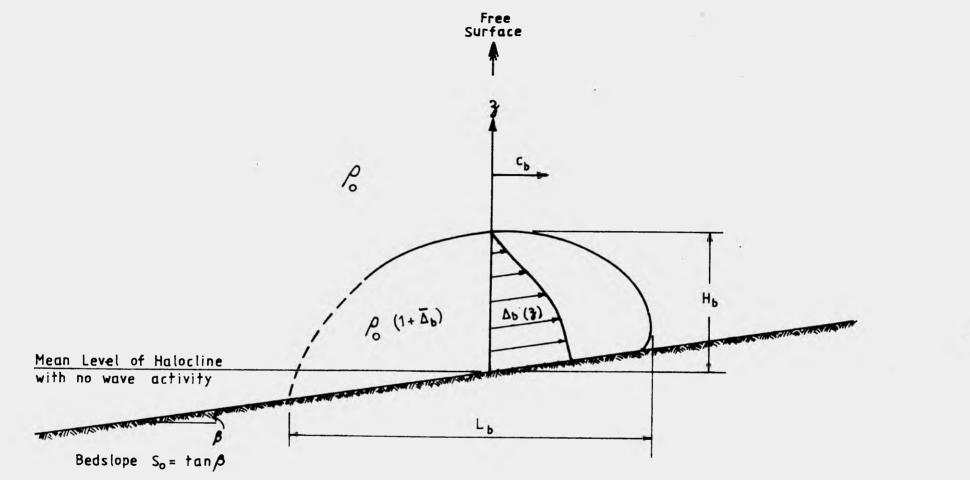


FIGURE 16.



Idealisation of an Internal Wave at Breaking

.

Figure (17) also shows the dominant parameters which describe an internal wave at breaking. The energy of a wave at breaking (E_b) may be expressed as:

$$E_{b} = E_{k} + E_{p}$$
(15)

where E_p = the potential energy of the wave and E_k = the kinetic energy of the wave which can be expressed as:

$$E_{k} = \frac{1}{2} \rho A_{b} (1 + C_{v}) c_{b}^{2}$$
(16)

where $A_b =$ sectional area of the 2-dimensional wave at breaking, $c_b =$ wave celerity at breaking where it was observed that the average velocity of fluid particles within the wave at breaking was very close to the phase speed of the wave, and $C_v =$ virtual mass coefficient which is given by $M_v/\rho A$ where M_v is the virtual mass of the broken wave form

The virtual mass coefficient allows for the motion (and hence kinetic energy) which is induced in the surrounding fluid by the the motion of the broken wave. It will be shown later in this section that a Froude number (F) can be expressed as $c/(g'H)^{1/2}$. Squaring the Froude number and evaluating at the point of breaking gives:

$$\mathbb{F}_{b}^{2} = c_{b}^{2}/g_{b}^{\prime} \mathbb{H}_{b}$$
(17)

where

 $g_{\rm b}' = \Delta_{\rm b}g$

in which
$$\Delta_b = \frac{1}{H_b} \int_{z=0}^{H_b} \Delta_b(z) dz$$

and $\Delta_b(z)$ = the vertical distribution of density excess within the wave at breaking.

Defining A in analogous terms to Equation (6) gives:

$$A_{b} = S_{1}H_{b}^{2}$$
(18)

Substituting for A and c_b^2 from Equations (17) and (18) into Equation (16) yields:

$$E_{k} = \frac{1}{2}\rho g_{b}' S_{1} F_{b}^{2} (1 + C_{v}) H_{b}^{3}$$
(19)

The gravitational potential energy is given by:

$$\mathbf{E}_{\mathbf{p}} = \rho \mathbf{A}_{\mathbf{b}} \mathbf{g}_{\mathbf{b}}' \mathbf{z}_{\mathbf{b}}$$
(20)

where z_b = the elevation of the centroid of density excess within the breaking wave above the mean level of the quiescent halocline.

 z_b is a function of the shape of the breaking wave and the vertical density distribution therein. z_b may be expressed in terms of the wave height at breaking as:

$$z_{b} = \chi H_{b}$$
(21)

Where χ is given by:

$$\chi = \frac{\left[\int \int zd(g'A)\right]_{b}}{g_{b}'H_{b}A_{b}}$$
(22)

Substituting Equations (18) and (21) into Equation (20) yields Equation (23), an expression for the gravitational potential energy at breaking in terms of the wave height (H_b) and effective gravity (g_b') at breaking.

$$E_{p} = \rho g_{b}' \chi S_{1} H_{b}^{3}$$
(23)

The addition of Equations (19) and (23) gives the total energy at breaking $(E_{\rm b})$ as:

$$E_{b} = \rho g_{b}' S_{1} H_{b}^{3} [\frac{F_{b}^{2}}{2} (1 + C_{v}) + \chi]$$
(24)

Our earlier assumption that energy is conserved up to the point of breaking gives:

$$E_{b} = E_{1}$$
(25)

Substituting for E_{b} and E_{l} from Equations (24) and (14) into Equation (25) yields:

$$\rho g_{b}' S_{1} H_{b}^{3} \left[\frac{IF_{b}^{2}}{2} (1 + C_{v}) + \chi \right] = \rho g_{1}' H_{1}^{2} \lambda_{1} / 8$$
(26)

If one now divides Equation (26) by $\rho g_b S_1 [(1 + C_v) \mathbb{F}_b^2/2 + \chi] H_1^3$ and takes the cube root, Equation (26) becomes:

$$\frac{H_{b}}{H_{l}} = \frac{1}{K_{b}(H_{l}/\lambda_{l})^{1/3}}$$
(27)

where
$$K_{b} = \left\{ 8S_{1} \frac{g_{b}'}{g_{1}'} \left[\frac{(1 + C_{v}) \mathbb{F}_{b}^{2}}{2} + \chi \right] \right\}^{1/3}$$
 (28)

Equation (27) gives the breaker height index (H_b/H_1) for internal waves as a function of the wave steepness prior to breaking (H_1/λ_1) and K_b as defined above.

2.5 Run-Up of an Internal Wave after Breaking

2.5.1 The Equation of Motion

wl

aı

The equation of motion parallel to the lower boundary for the idealized flow pattern which was shown in Figure (10) is:

$$\frac{d}{dt} \int_{A} (\rho u) dA - \Sigma F = 0$$
(29)
here $\frac{d}{dt} \int_{A} (\rho u) dA = rate of change of momentum
hd $\Sigma F = the sum of the forces acting parallel
to the lower boundary.$$

Equation (29) may be written in terms of the volume of fluid (per unit crest width) within the broken wave, its celerity and virtual mass, and the component forces acting in the direction of motion as:

$$\frac{d}{dt} \rho Ac(1 + C_v) + \Delta \rho g AS_o + \frac{C_d \rho c^{2} H}{2} + \frac{S_2 \rho q_i^{2}}{h_i} = 0$$
(30)
(i) (ii) (iii) (iv)

- term (ii) = the component of the gravity force acting parallel to the lower boundary.
- term (iii) = the combined body and frictional drag forces in which C_d
 is a combined drag coefficient, as described in Appendix
 (4).
- term (iv) = a force acting on the wave which is equal to the momentum
 flux contribution from the backflow of the previous wave.
 S₂ is a shape factor expressing the momentum in the back flow and is given by:

$$S_{2} = \frac{h_{i}}{q_{i}^{2}} \int_{z=0}^{h_{i}} [(u_{i}(z))]^{2} dz$$
(31)

Dividing Equation (30) by ρ , substituting for Δg from Equation (5) and for A from Equation (6) gives:

$$S_1 (1 + C_v) \frac{d}{dt} cH^2 + S_1 S_0 g'H^2 + \frac{C_d c^2 H}{2} + \frac{S_2 q_1^2}{h_i} = 0$$
 (32)

In a frame of reference which moves with the wave with velocity c, d/dt may be expressed as:

$$\frac{d}{dt} = \frac{\partial}{\partial t} + c \frac{\partial}{\partial x}$$
(33)

If it is assumed that the flow is quasi steady, then $\partial/\partial t \ll c \partial/\partial x$ and the partial differential becomes a total differential as given in Equation (34).

$$\frac{d}{dt} = c \frac{d}{dx}$$
(34)

Equation (32) may now be expanded using the relationship in Equation (34) to give:

$$2S_{1}(1+C_{v})Hc^{2}\frac{dH}{dx} + S_{1}(1+C_{v})H^{2}c\frac{dc}{dx} + S_{1}S_{0}g'H^{2} + \frac{C_{d}c^{2}H}{2} + \frac{S_{2}q_{i}^{2}}{h_{i}} = 0$$
(35)
(i) (ii) (iii) (iv) (v)

In Equation (35), the first term is proportional to the rate of change of momentum resulting from a change in wave height during run-up. The second term is proportional to the rate of change of momentum resulting from a change in wave celerity during run-up. The third and fourth terms are respectively proportional to the gravity and drag forces acting on the wave parallel to the lower boundary. The fifth term represents a force, proportional to that resulting from the momentum in the approaching backflow from previous waves.

2.5.2 Order of Magnitude Analysis

At this stage an order of magnitude analysis is to be undertaken with the object of facilitating an analytic solution identifying the dominant terms in Equation (35). These are then included in a simplified model which will be used to describe the variation in wave height and celerity with stage of run-up. The approximate magnitudes of the five terms in Equation (35) were evaluated by substituting mean values for experimental parameters from Appendix (1) and by using the following approximations:

> $O(dH/dx) \sim O(H/x)$ $O(dc/dx) \sim O(c/x)$ $O(S_2) \sim 1$ $O(q_i) \sim O(A/T)$

where T = the wave period and x = a distance measured along the sloping shelf from the breakpoint

The magnitude of the terms in Equation (35) are given in Table (2).

TABLE 2. Magnitude of the Terms in Equation (35)

Term	Magnitude			
(i)	4×10^{-5}			
(ii)	2×10^{-5}			
(iii)	2×10^{-5}			
(iv)	2×10^{-5}			
(v)	2×10^{-6}			

Table (2) shows that the magnitudes of the first four terms are approximately equal and an order of magnitude greater than the fifth term (the momentum of the back flow). As a first approximation it can be assumed that the contribution from the fifth term in Equation (35) can be neglected. The dominant terms in Equation (35), after dividing by $g'H^2$ now become:

$$2S_{1}(1+C_{v})\frac{c^{2}}{g'Hdx} + S_{1}(1+C_{v})\frac{c}{g'dx} + S_{1}S_{0} + \frac{C_{d}}{2}\frac{c^{2}}{g'H} = 0$$
(36)
(i) (ii) (iii) (iv)

2.5.3 Evaluation of Similarity Solution

If we assume a similarity solution exists for Equation (36) such that $c \propto x^a$, $H \propto x^b$, $g' \propto x^e$ and hence $dc/dx \propto x^{(a-1)}$ and $dH/dx \propto x^{(b-1)}$ then the laws of similitude when applied to Equation (36) give the following relationships:

	2a - e - 1 = 2a - e - b	[from terms (i) and (iv)]
which gives	b = 1	(37)
and	2a - e - 1 = 0	[from terms (ii) and (iii)]
which gives	2a - e = 1	(38)

If we define a Froude Number (F) as in Equation (39), then F is proportional to $x^{[a-(e/2)-(b/2)]}$ which, using the relationships in Equations (37) and (38) reduces to x° (=1).

$$\mathbf{F} = c/(g'H)^{1/2}$$
(39)

It follows that to the first order of approximation, the Froude number is constant during run-up. If we assume that the system is two layered with no mixing, then g' is constant and e is equal to zero. The values of a and b are thus 1/2 and 1 respectively which gives c $\propto x^{1/2}$ and H $\propto x$.

2.5.4 Derivation of Run-up Relationships

Equation (39), when differentiated with respect to x and re-arranged gives:

$$c\frac{dc}{dx} = \frac{\mathbf{I}\mathbf{F}^2}{2} \mathbf{g}' \frac{d\mathbf{H}}{d\mathbf{x}}$$
(40)

where \mathbf{F} and \mathbf{g}' have been assumed to be independent of \mathbf{x} as described above. Equation (36) may now be written in terms of \mathbf{F} by using the relationships in Equations (39) and (40) as:

$$5S_{1}(1+C_{v})\mathbb{F}^{2}\frac{dH}{dx} + 2S_{1}S_{0} + C_{d}\mathbb{F}^{2} = 0$$
(41)

Equation (41) when divided by $5S_1(1 + C_v)F^2$ and integrated between the point of breaking (x = 0, H = H_b) and a point a distance (x) up the slope gives:

$$\int_{H_{b}}^{H} dH = \frac{-1}{5(1 + C_{v})} \left[\frac{2S_{o}}{\mathbb{F}^{2}} + \frac{C_{d}}{S_{1}} \right] \int_{0}^{x} dx$$
(42)

Equation (42) when evaluated and re-arranged gives:

$$\frac{H}{H_b} = \left[1 - \psi \frac{x}{H_b}\right] \tag{43}$$

where
$$\psi = \frac{1}{5(1 + C_v)} \left[\frac{2S_o}{\mathbb{F}^2} + \frac{C_d}{S_1} \right]$$
 (44)

Equation (43) describes the variation in height of a broken internal wave versus stage of run-up as it propagates up a gentle slope.

An expression for the wave celerity during run-up can now be determined. Noting that the value of F is constant during run-up, and that g' has been assumed constant, Equations (17) and (39) can be combined to give an expression for the wave celerity during run-up as:

$$\left[\frac{c}{c_{b}}\right]^{2} = \frac{H}{H_{b}}$$
(45)

Substituting for H/H_b from Equation (43), Equation (45) yields:

$$\frac{c}{c_b} = \left[1 - \psi \frac{x}{H_b}\right]^{1/2}$$
(46)

Equation (46) relates the variation in celerity of a broken internal wave to the stage of run-up.

3. EXPERIMENTAL APPARATUS

3.1 Requirements

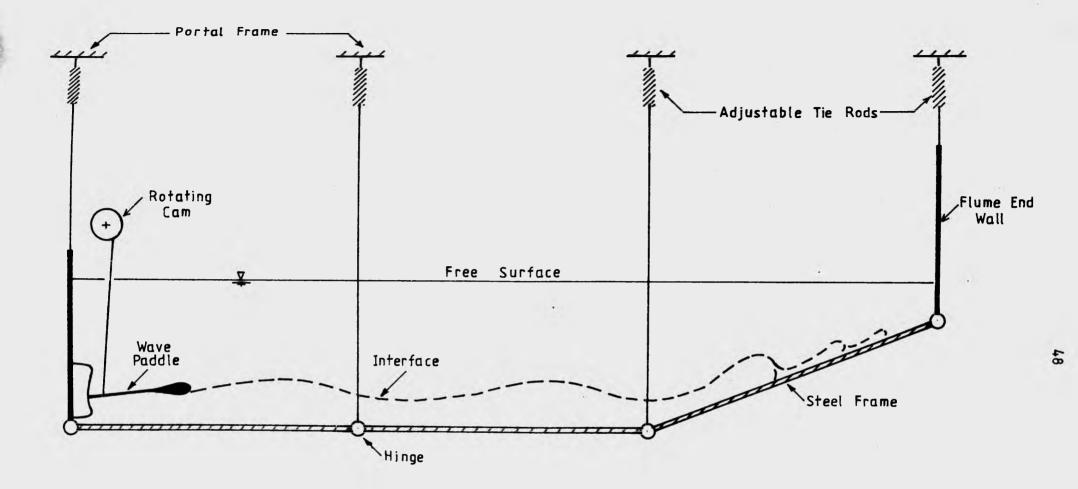
The basic requirements for the experimental apparatus were:

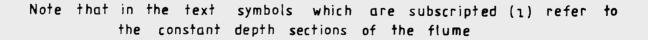
- A simple, inexpensive system in which monochromatic internal waves of variable period and amplitude could be continuously generated, and
- A flume section far from the wavemaker which simulated the continental shelf and could be adjusted to any slope, and
- The ability to qualitatively observe and quantitatively measure the changes which an internal wave would undergo as it encountered and shoalled upon a gently sloping bed.

3.2 Wave Flume

The wave flume which is shown schematically in Figure (18) was comprised of 3 sections, each 6m long, 590mm internal width and 760mm deep. One side and the bottom of each section was constructed of marine plywood, while the other side was constructed of 12mm perspex that gave a relatively uninterrupted qualitative view of the internal wave activity from wave generation to decay at the limit of run-up on the sloping section.

The flume walls were supported in suspended steel frames, each of which was hinged to the adjacent section and supported at the hinge via adjustable tie rods to an overhead portal frame. The flume sections could





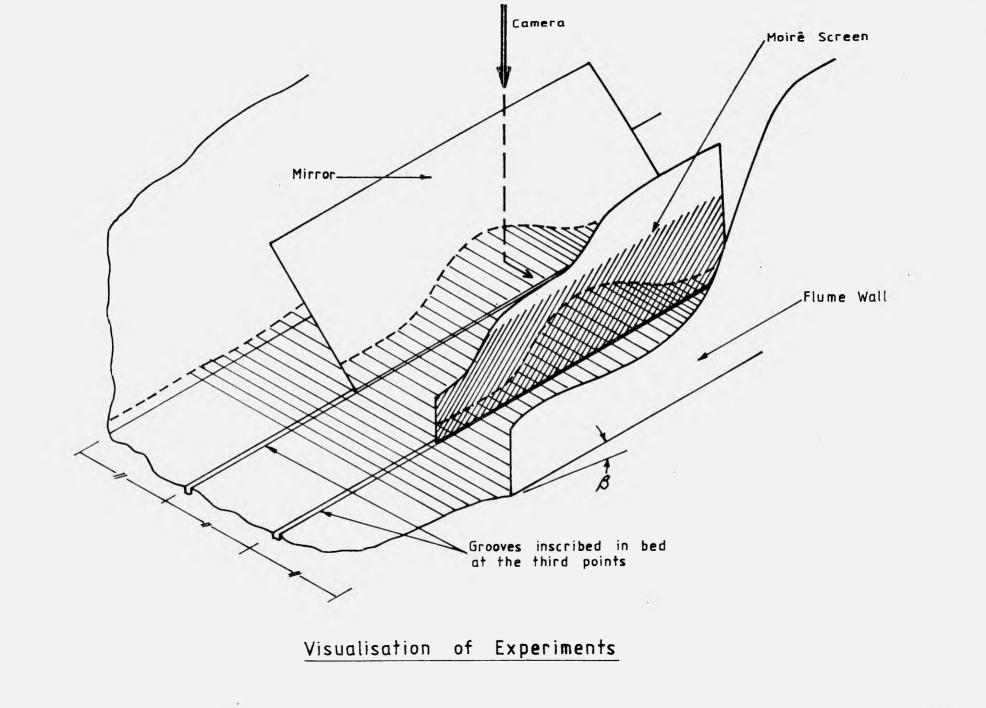
Schematic of Wave Flume

therefore be set to different slopes as required for the experiments. The centre section and that containing the wavemaker were horizontal which enabled the wave form to travel the maximum possible distance and thus to stabilize into a "non-forced" wave before the region of study. The third section was set to slopes of 0.030 and 0.054 compared with slopes of 0.005 to 0.01 which are typical of a continental shelf. This was necessitated by space limitations as a flatter slope would not produce a sufficient change in elevation over the length of the sloping section, the result of which was that the shoaling and breaking processes were not completed in the region of observation and measurement and the breaking wave did not completely dissipate before impinging upon the end of the flume. The bed slopes were however considered to be befitting for the prototype shoaling and breaking processes to be duplicated.

Two grooves were inscribed longitudinally in the bed of the sloping section at the third points (Figure 19) to provide alignment and support for the Moiré screen and mirror as will be described in Section (3.5). As a photographic aid black contact adhesive vinyl sheeting was secured to 0.5mm thick galvanized steel sheet which was then placed along the centre third of the bed in the sloping section. The vinyl sheeting also electrically insulated the steel sheet from the conductivity probes. Distance markers which were painted upon the black surface using white high gloss paint were clearly visible in the photographs (Figure 20) and were resistant to attack by the salt water.

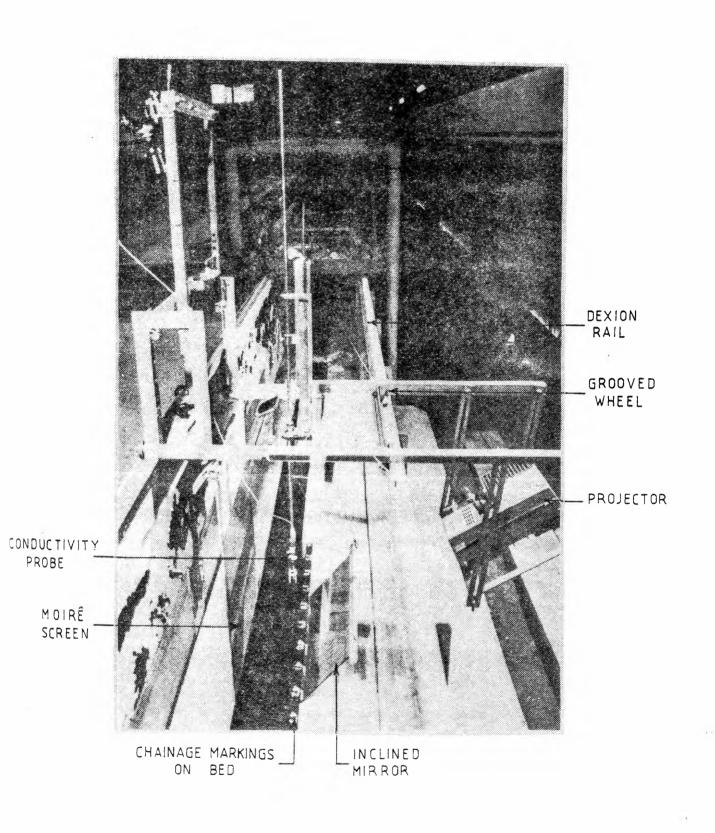
3.3 Mixing and Filling System

In order to minimise the thickness of the halocline separating the saline and fresh water layers, the saline solution was first mixed in a separate tank and then injected under the fresh water layer.



50

.



Equipment Trolley

The mixing tank dimensions were $1,370 \text{ mm} \times 920 \text{ mm}$ which gave a volume of 1.4m^3 when filled to the maximum depth of 1.1 m. After the salt and fresh water were placed in the mixing tank, the salt was dissolved with the aid of a 370 W industrial stirrer that was placed off centre in the tank to reduce solid body rotation of the fluid. Once mixed, the discharge of saline solution into the flume was adjusted to minimise mixing at the saline solution/fresh water interface by controlling a 25 mm brass valve on the outlet pipe.

After filling, (or at any stage during the experiment), the thickness of the halocline could be reduced by selective withdrawal using three siphons which could be lowered into the flume and located at the level of the halocline. The siphons each consisted of two sheets of 200 mm diameter stainless plate that were aligned in the horizontal plane 2mm apart with a 10 mm diameter stainless tube to withdraw fluid from their centre. The withdrawal tubes were connected to a 200 W self priming pump via flexible PVC tubing and a 3 to 1 junction.

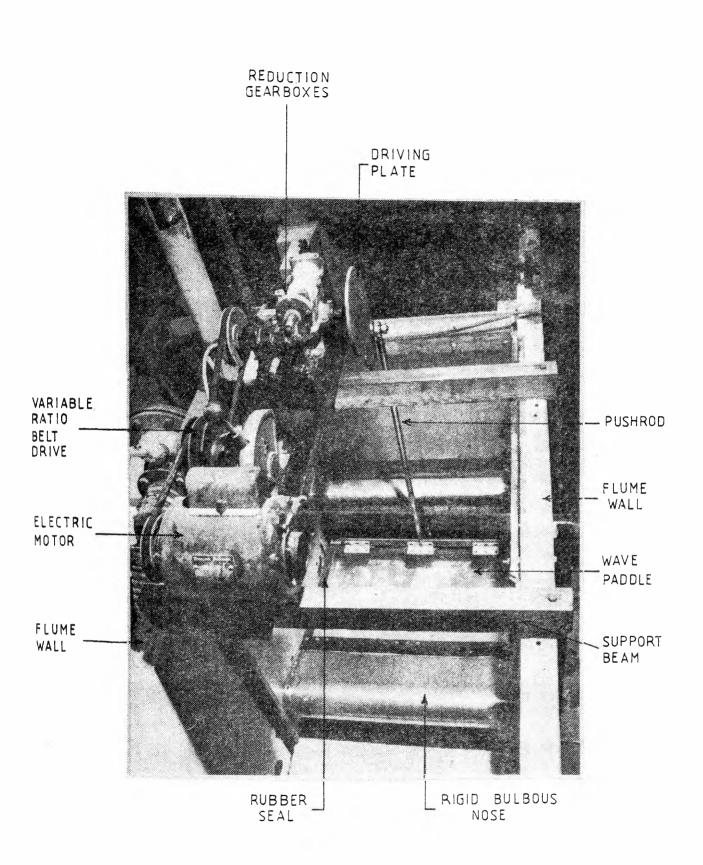
If it was desired to increase the level of the free surface after injection of the saline layer, then fresh water was added by three filling floats in a manner so as not to disturb the halocline. Each float consisted of 10mm thick x 400mm diameter expanded styrene foam which was mounted on a 410mm diameter masonite base. Fresh water was supplied via three 10mm diameter PVC tubes to the floats. The addition of horsehair on the upper surface of the floats created sufficient headloss to destroy the velocity head from the filling tubes thus producing a relatively even discharge in all directions. As the floats lay just below the free surface the filling water attained no vertical velocity component as it flowed onto the free surface.

3.4 Wave Generator

The wave generator had to satisfy several requirements. The driving mechanism had to operate over the desired frequency range and be sufficiently powerful and smooth so as not to induce excessive vibrations either in the flume on which it was mounted or in the wave paddle itself. The wave paddle had to produce internal waves in the desired amplitude range whilst not causing any significant degree of mixing in the halocline in the vicinity of the paddle. Finally, the system had to be reliable, corrosion resistant below the water line and able to produce internal waves at any desired elevation.

Figure (21) shows the final design. The entire drive mechanism was rigidly supported above one end of the flume on 5 mm steel plate that sat on two 65 mm x 40 mm wood beams spanning the flume walls. The drive mechanism consisted of a 560 W electric motor operating at 1,440 RPM. The motor shaft was connected to a variable ratio belt drive and then to a gear box giving a total reduction of 250:1. The belt drive provided continuous frequency control from \approx 1:2 to 2:1. Attached to the output shaft of the final gearbox was the driving plate which rotated at frequencies of 0.05 to 0.20 hertz, depending on the setting of the variable belt drive. The paddle assembly was self-contained and housed in a three-sided perspex box which was lowered into the flume and bolted to the flume walls at the desired elevation.

The wave paddle itself consisted of a 14 mm thick perspex plate hinged to a rigid bulbous nose, the purpose of which was to prevent mixing in the halocline at the wavemaker. To obtain an effective seal between the paddle and the box 3 mm thick rubber strips were glued to the paddle edges. The paddle was driven by a stainless steel pushrod hinged at the paddle and



Wave Generator

connected to the driving plate by a 12mm FAG maintenance free rod end which allowed for small misalignments in the driving mechanism and paddle assemblies. For corrosion resistance all parts below the waterline were constructed in stainless steel, perspex or PVC.

3.5 Equipment Trolley

The wave, after breaking on a gently sloping shelf would run up a distance of $O(H_b/S_0)$ which corresponded to 1-2m in the model, and it was therefore not practical to collect data on the whole sequence of events simultaneously. Consequently, a mobile equipment trolley was designed and constructed, the purpose being to track the wave during run-up, and thus collect continuous data on the wave characteristics from the point of breaking to the limit of run-up.

The unit, which is a rigid frame of brass angle and aluminium sheet was shown in Figure (20). To achieve mobility the system was equipped with drive cables, a variable speed motor and grooved wheels which ran on two Dexion rails mounted longitudinally on the flume walls. However, during preliminary experiments, it was observed that the development of the boundary layer along the flume walls was significantly affecting the waveform.

The broken wave within about 10 cm of the wall would lag behind and was lower than the wave in the centre of the flume. When viewed from a distance from one side a primary double image and fainter secondary images were observed. The system was therefore modified so that only the image in the centre one-third of the flume would be recorded. Two grooves were inscribed in the bed at the third points (Figure 19), and depending on the stage of the experiment, either a Moiré screen or a black grid was located at one of these points and an inclined mirror at the other point. The

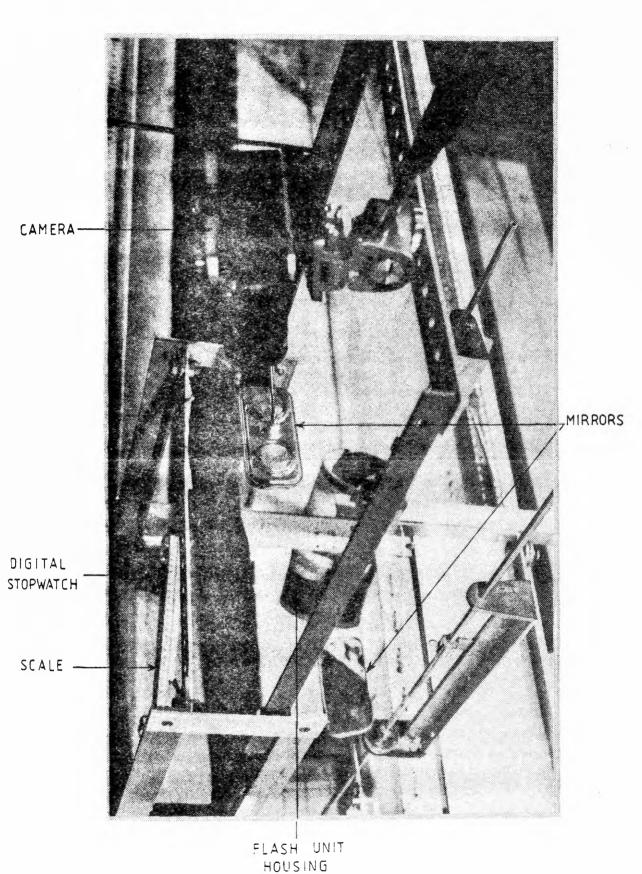
Moiré screen consisted of an array of parallel diagonal lines traced on to a plane screen. When the screen is viewed through a medium in which there are variations of refractive index (caused in this case by varying salt concentrations) the lines appear to distort, the distortion being a maximum where the salinity gradients are a maximum. This technique enabled visualisation of flow structures and a qualitative estimate to be made of turbulence scales within the stratified region as described in Section (2.2). The screen/grid and mirror were now the flow boundaries. Unfortunately, disturbances caused to the wave as a result of using the screen/grid/mirror system to track the wave necessitated the abandonment of a mobile system. Data was henceforth collected at discrete intervals up the slope.

3.6 Photographic Equipment

The photographic equipment consisted of the following:-

- OLYMPUS OM-In 35mm camera with OLYMPUS Motor Drive 1 and OLYMPUS M.AC control unit
- NIKON AC powered Repeating Flash Unit
- POPULAR 303S Flash Unit
- An LCD digital stopwatch
- HANIMEX Syllabus 2000 Slide Projector.

Figure (22) shows, attached to the trolley, the camera which was fitted with an f3.5, 135mm lens (to reduce parallex error) plus a 7mm auto extension tube to reduce the minimum focusing range. The flash units were



57

Photographic Equipment

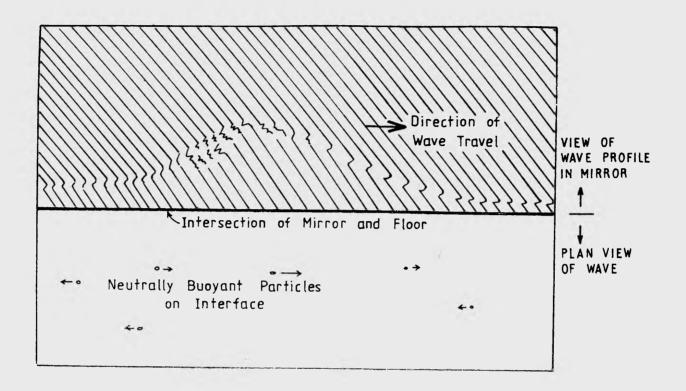
supported in a watertight PVC housing just below the free surface in order to eliminate flash bounce from the water surface which in preliminary trials was found to be detrimental to the quality of the photographs. The projector was suspended from the trolley outside the flume, and angled such that the light beam passed through the perspex wall below the free surface to eliminate reflections for the reasons stated above. A LCD digital stopwatch, when viewed through a system of mirrors (to produce the same length focal path for photographic purposes) provided a time base for the experiments.

The main mirror was positioned in one of the slots in the bed, and the angle adjusted by tensioning stainless steel support cables. A Moiré screen (or black grid as necessary) was placed vertically in the other slot and clamped to the trolley with spring clamps. The mirror/Moiré screen system was shown diagramatically in Figure (19). A schematic of the image recorded by the camera is shown in Figure (23).

A lamp was attached to the trolley to provide general illumination immediately before and after the "flash" section of the experiment. During this "flash" section complete darkness (excepting the illumination provided by the flash units) was required, or the background light would "wash out" the image produced by the flash.

3.7 Conductivity Probes and Meter

Four conductivity probes, details of which are described in Appendix (3), were attached to adjustable vertical support rods. The support assemblies were mounted on sliding trolleys which enabled the measurement of conductivity, and hence salinity and density anywhere in the flume.



Schematic of Image Recorded by Camera

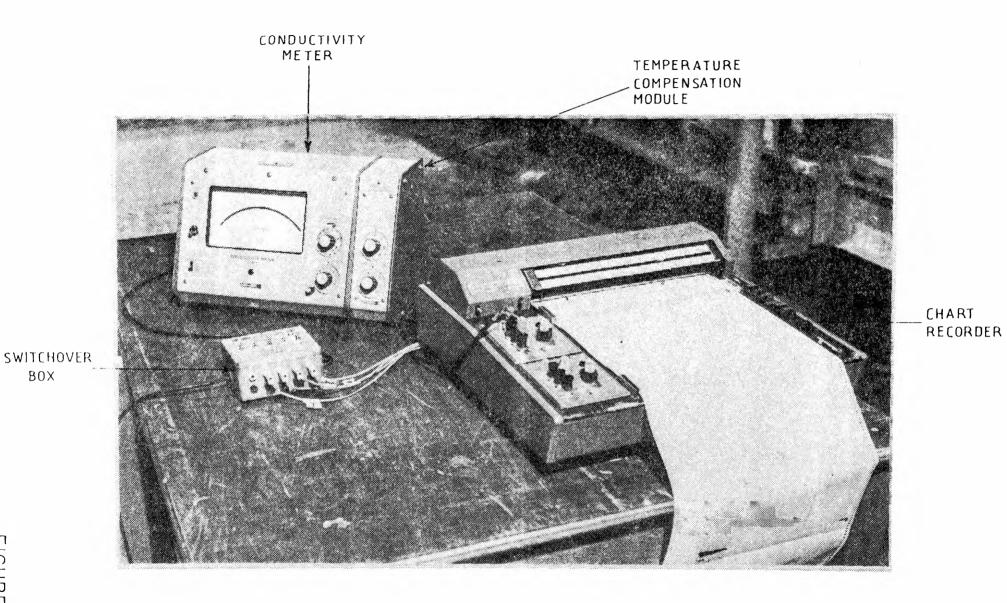
The probe modules were connected by co-axial cable to a switch box and thence to a RADIOMETER CDM3 Conductivity Meter with an integrated CDA100 Temperature Compensation Module (Figure 24). As conductivity and density are both functions of temperature, temperatures were measured with a calibrated thermistor probe as shown in Figure (25).

The meter output fed a LEEDS AND NORTHRUP Dual Pen Strip Chart Recorder which provided a permanent record of conductivity readings during an experiment. The output speed of the chart was calibrated and found to be within 1% of true, thus providing an effective time base for the records.

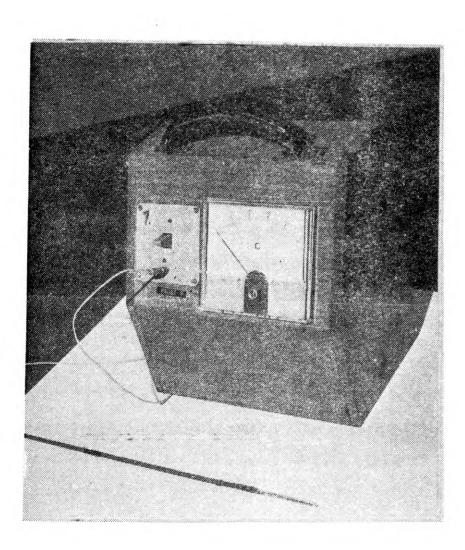
The conductivity meter was powered through an isolating transformer to avoid problems with earth looping through the flume. Earth looping resulted in calibration problems if the meter was earthed directly through the power mains.

3.8 Density Measurement

Although the conductivity probes were calibrated prior to each experiment, provision was also made for withdrawing fluid samples from the flume for independent density evaluation. A vertical array of 3mm diameter outlets were located in the perspex flume wall above the junction of the sloping and horizontal bed sections. Samples were taken from each outlet and the density measured using a calibrated hydrometer which could be read to 0.0005 in the range 0.980 to 1.053.



Conductivity Meter and Chart Recorder



Thermistor Probe



EXPERIMENTAL TECHNIQUE

4.1 Experimental Procedure

On the day prior to an experiment the saline solution mixing tank was filled with fresh water to the required level and a measured quantity of salt added. The stirring rod and impellers were then used to mix the salt into solution. The angle of the sloping section of the flume was adjusted as necessary using two \times 5 tonne hydraulic jacks. The flume was flushed out and filled with fresh water to the required level. The water surface was then covered with floating PVC bubble blanket which minimized evaporation and prevented dust from contaminating the flume. It was necessary to keep the flume filled to approximately the same level continually or the ageing timbers of which it was constructed would move causing the flume to leak.

The wave period for the experiment was set by timing 10 revolutions of the wave generator with a digital stopwatch. The pushrod offset was then set to a calculated value to produce the required wave height for a particular experiment.

On the morning of the experiment the salt water filling valve was opened and the flow into the flume regulated visually to minimise mixing as the saline solution flowed under the fresh water. Filling was usually completed in about one to two hours.

As the flume filled the final preparations were undertaken. The camera was mounted on the trolley, its operation and film supply checked. The flash units were mounted and their operation checked. The conductivity probes were checked in standard solutions of known temperature to obtain an

updated calibration curve. Once filling (and siphoning as necessary) were completed and any long period oscillations created by the filling process had ceased, the probes were placed in the flume, zeroed vertically with respect to the bed and a vertical conductivity profile recorded at the junction of the horizontal and sloping bed sections. Samples were taken and their density measured with the hydrometer. This provided an in-situ calibration and a check against any errors in the conductivity profile measurement.

Prior to wave generation the visual level of the interface was recorded, together with a temperature scan over the depth. The visual interface corresponded approximately to the 5% density excess level which is defined in Section (5). The temperature varied less than about $1/2^{\circ}$ centigrade except for the surface 5 to 10 cm where evaporative cooling reduced the temperature by up to about 2° C. The temperature in the region of interest was constant and was found to remain steady during the course of the experiment.

4.2 Executing the Experiment

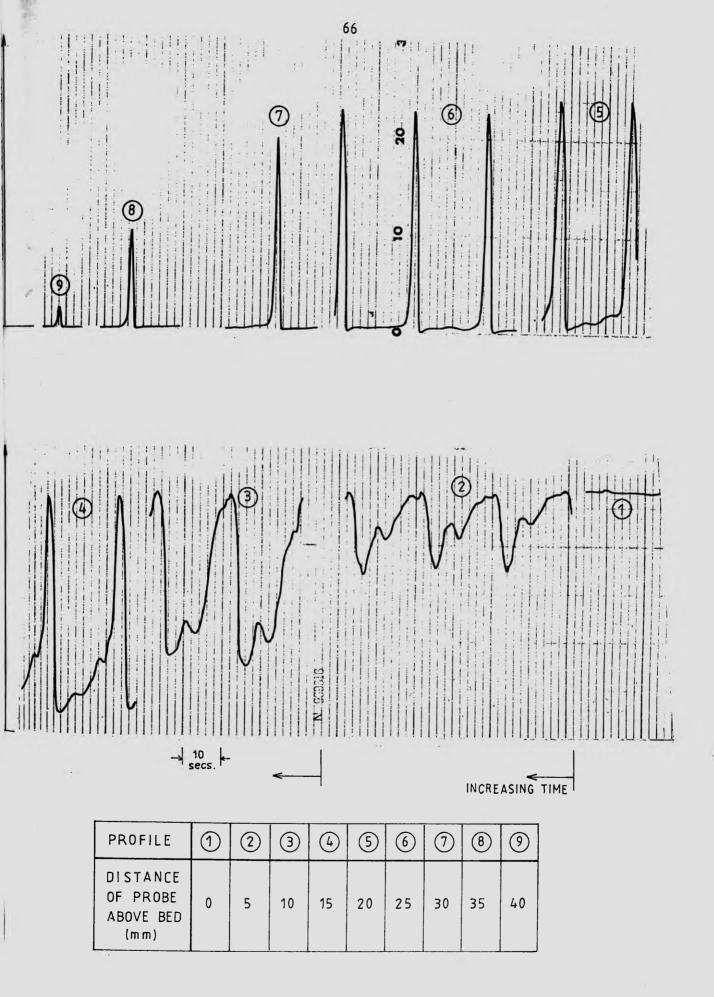
After the wave generator had been running for about 10 minutes and the wave form had stabilized, data collection was commenced. The wave height, defined as the vertical excursions of the isopycnals between the 20% and 80% density excess levels and the wave celerity in the constant depth region of the flume were determined using the output from two conductivity probes. Section (5) gives a detailed description of this technique. The wave celerity in the sloping section of the flume was measured by visually tracking the wave, and at each 0.1m chainage a remote switch operated to produce a mark on the chart recorder output.

After visually determining the region of interest, chainages were selected for data collection. Vertical conductivity profiles were collected by recording the output from a conductivity probe at discrete vertical steps for a given chainage. Figure (26) shows a sample record. This process was repeated at various chainages until the broken wave had reached its limit of run-up.

The wave was then photographed against a Moiré screen at the same chainages, with about five sequential images being recorded as the wave passed through the camera's field of view. As well as providing a qualitative picture of the wave, the sequential Moiré screen photos (each showing the time to 0.01 sec) also provided a check on the wave celerity as it passed through the frame.

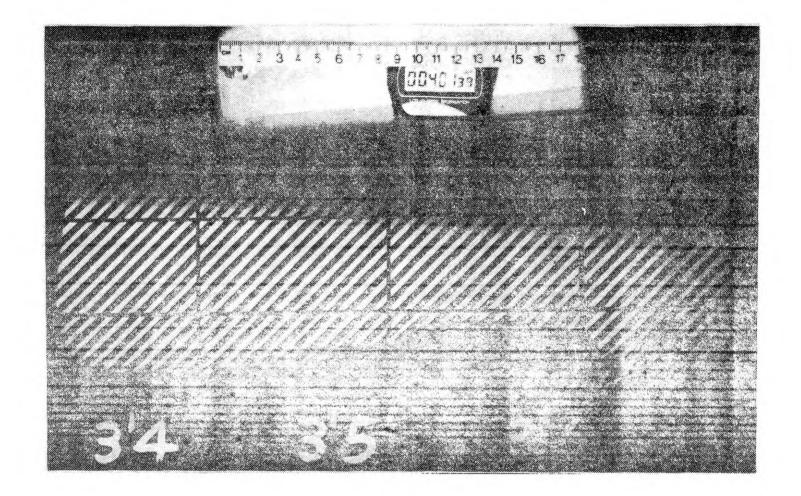
Figure (27) shows a typical Moiré screen image, including the scale, timer and chainage markings, from Experiment No. (6).

Particle trajectories were obtained using neutrally buoyant particles, (details are described in Appendix 2) which were previously immersed in a wetting solution. These were placed just below the free surface by hand. The wetting agent prevented the formation of air bubbles on the particles and had the added advantage of decreasing the surface tension, causing any dust particles on the surface to disperse, leaving a clear surface through which to photograph. The particles would fall to their equilibrium level where they would then be photographed. The particles were photographed using an open shutter on the camera and illumination was provided by a flash unit firing at 4 flashes/sec for about 5 seconds. A slave flash was also fired simultaneously at the beginning of the sequence to provide a recognisable starting point on each particle trace.



<u>Sample Record of</u> <u>Raw Conductivity Probe Output</u> (From Experiment No. 5.)

FIGURE 26.



Moirê Screen Image Showing Wave,Scale, Timer and Chainage Workings

(From Experiment No. 6.)

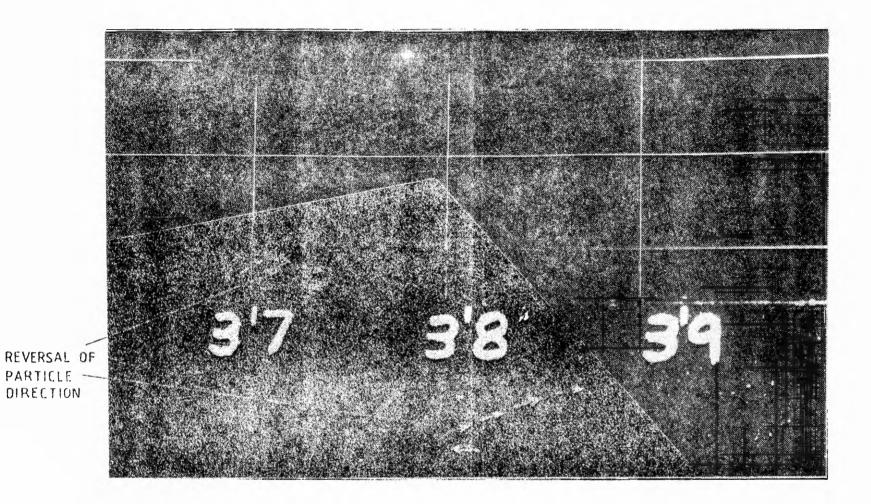
Each trace consisted of about 10 to 20 images of a single particle, the first image being brighter than the others. This enabled the direction of motion to be determined, and knowing the time interval between flashes, particle velocities could be readily obtained. Figure (28) shows a typical image from Experiment No. (3). The apparent distortion of the lower horizontal grid line is a result of the change in refractive index (caused in this case by varying salt concentrations) as the wave moves through the field of view.

The wavemaker was then turned off, and after the fluid became quiescent, a vertical conductivity profile was recorded at the junction of the sloping shelf and horizontal bed sections. Sample bottles were filled and the density measured with a calibrated hydrometer as before. This provided a further updated conductivity probe calibration curve and adjustments to the recorded data were made as necessary.

4.3 Post-Experimental Procedure

The conductivity probes were removed from the flume, rinsed and placed in distilled water. This helped to preserve the platinization and to minimize any corrosion which the salt water may have initiated.

The films were processed by the author the same night in the laboratory's darkroom. This was necessary as, due to the low light level in the experiments, the film had to be rated (and hence developed) at 1600 ASA, which meant that any minute amount of stray light (for example under the darkroom door) during processing could fog the film. The added advantage of immediate processing was that any problems with the photography could be corrected immediately, and sections of the experiment repeated as necessary.



Typical Neutrally Buoyant Particle Traces (From Experiment No. 3)

4.4 Optional Dye Injection

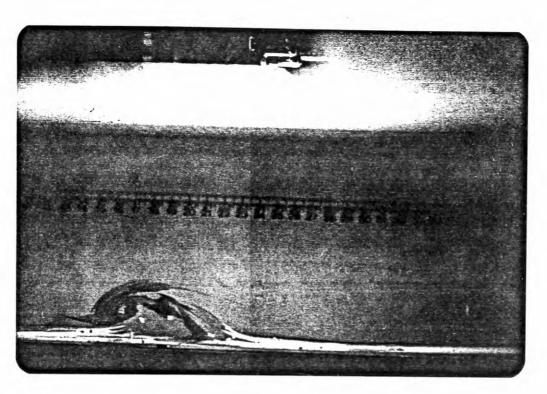
In order to produce a better qualitative record, at the conclusion of an experiment, the wavemaker was sometimes re-started and additional data recorded.

The camera was loaded with Kodak Ektachrome 400 ASA colour slide film. Dye, either a potassium permanganate solution or a blue food dye solution was injected into the wave using a long hypodermic needle and syringe. The wave was then photographed as it passed through the field of view of the camera.

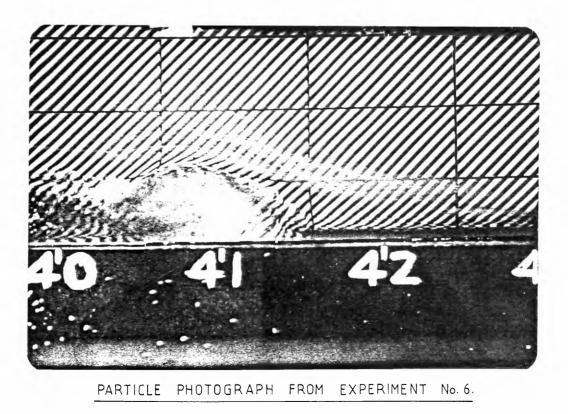
Neutrally buoyant particles, as described earlier, were spray painted various colours and placed in the flume. By setting the camera motor drive to 4 frames/sec it was possible to track the particles from one slide to the next, using their colour as well as position for correlation. In this manner, pathlines within the highly turbulent head vortex were obtained. Figure (29) shows typical dye and particle photos.

4.5 Preliminary Investigations

Prior to commencing the experiments described in this thesis several experimental methods were investigated and subsequently rejected. The original method for filling the flume was to mix the saline solution in the flume and then float the fresh water on top overnight. This method was later rejected as time consuming, difficult to control and undesirable because of the high degree of initial mixing, and hence thickening of the halocline which would result. Additionally, due to the ageing nature of the flume, if the water level was not kept relatively constant, the flume walls would move in or out (up to ~ lcm at the top) and the flume would



DYE PHOTOGRAPH FROM EXPERIMENT No. 1.



Dye and Particle Photos



leak necessitating continual monitoring to determine the level of the halo-

Hydrogen bubble wires were investigated as a means of velocity measurement but were rejected because of the high degree of turbulence found in the region of interest. The photographic system was originally designed with the camera on a variable speed trolley beside the flume, such that the camera would continuously track the wave as it shoaled upslope. This was rejected when 3-dimensional effects were discovered in the wave form, resulting in ambiguous "double" images being recorded.

5. DATA REDUCTION AND ANALYSIS

In this section we describe the procedures which were followed to evaluate the experimental parameters (as tabulated in Appendix 1) from the raw data which were collected during the experiments.

5.1 Measurements in the Constant Depth Section of the Flume

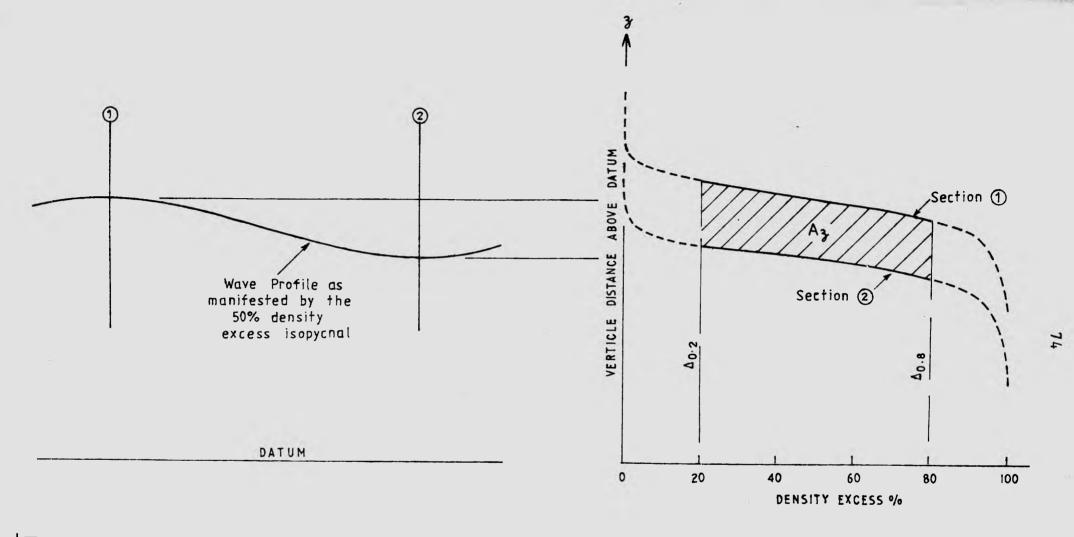
5.1.1 Wave Height

The wave height, which is defined as the mean excursion of the isopycnals in the range of density excess from 20% to 80% may be expressed mathematically as:

$$H_{1} = \frac{A_{z}}{z_{0.8} - z_{0.2}}$$
(47)

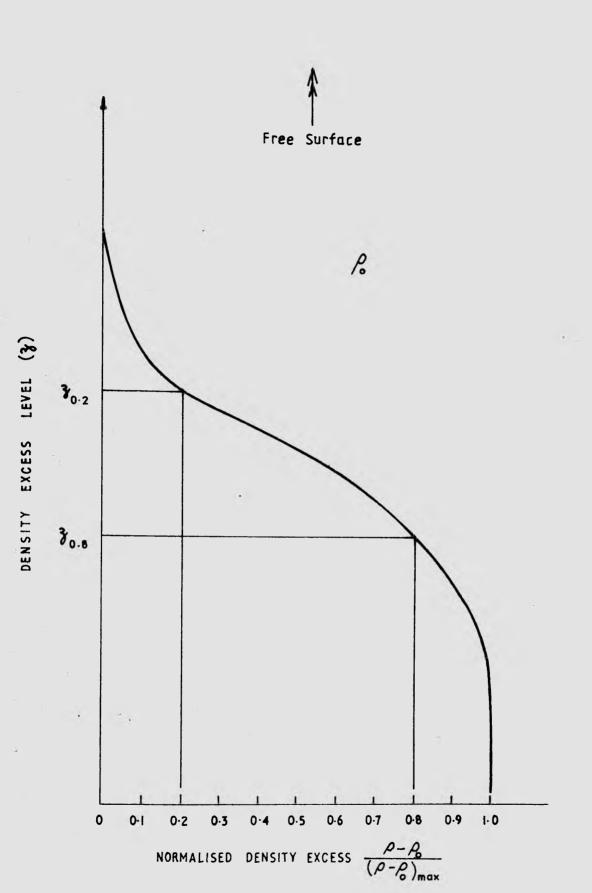
where A_z equals the area between the crest and trough density excess profiles within the range of density excess of 20% to 80% as defined in Figure (30) and

The wave height was defined as above in order to allow for the variation in density within the halocline as the model was not a true two layered system.



Definition Sketch for Wave Height Measurement in Constant Depth Section of the Flume

FIGURE 30.



Normalised Density Excess - Definition Sketch

FIGURE 31.

5.1.2 Wave Celerity

The wave celerity in the constant depth region of the flume was determined by timing the passage of an internal wave between two conductivity probes from which the wave crest could be readily identified. Note that, in order to ensure that the same wave crest was being sensed by both probes, the procedure was carried out twice with the probes being at two different spacings which enabled verification of the wave crest being sensed. The probe tips were placed at the 5% density excess level in the quiescent halocline.

In determining the celerity it was assumed that the wave celerity (c_1) was constant in this section and could therefore be expressed as:

$$c_{1} = \frac{\Delta x}{\Delta t}$$
(48)

where Δx = the (known) distance between the probes and

 Δt = the time for the wave to traverse the distance Δx .

Under wave action, the maximum elevation of the isopycnals, which corresponded to a crest produced the maximum conductivity at the respective probe. The two probes were connected to a changeover box with a common outlet into the conductivity meter and thence the chart recorder. By visual observation of the chart trace, the time at which the wave passed each probe was readily discernable, thus making it possible to manually change the input from each probe for successive waves, as shown in Figure (32).

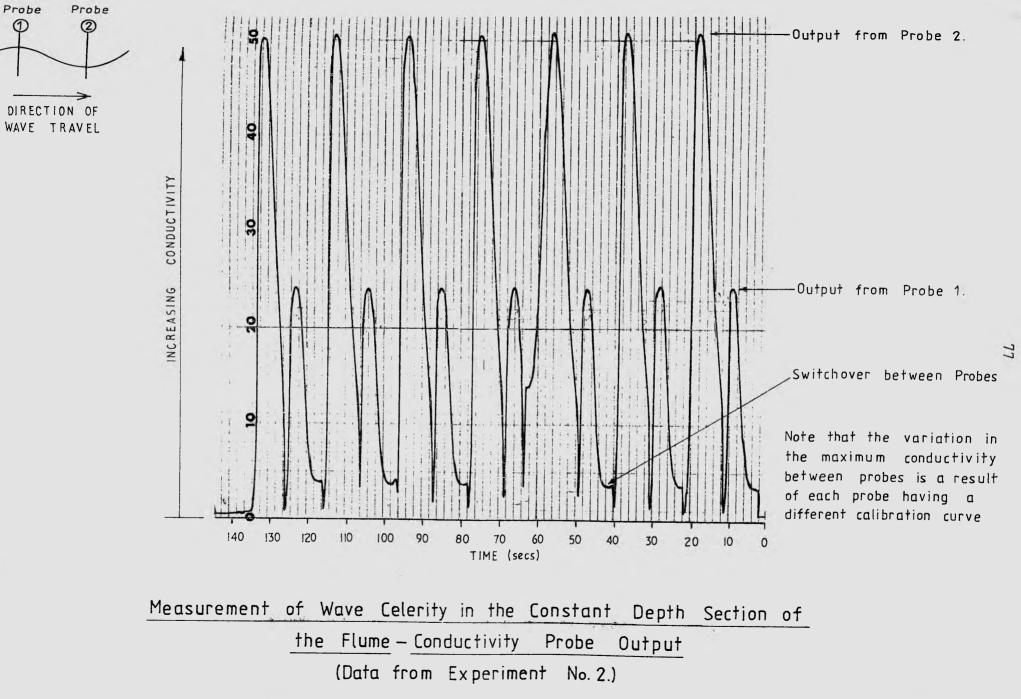


FIGURE 32.

5.2 Measurements on the Sloping Shelf After Breaking

5.2.1 Wave Celerity

As the celerity was continually changing as the broken wave propagated up the shelf, the method described in the previous section could not be used. A method, which could determine the instantaneous celerity was therefore devised, and is described below. The method utilised the fact that, at breaking, as a result of the strong shearing of the flow the interface (halocline) sharpens dramatically, becoming readily observable to the naked eye. From this point to the limit of run-up the broken wave was tracked visually, a remote button attached to the chart recorder being activated at predetermined chainages (usually every 100 mm).

78

As the paper feed on the recorder had been calibrated with a timing error of less than one per cent, it provided an accurate measure of the time for the wave to travel each 100 mm interval. A second order least squares polynominal regression of the form,

$$x = a_1 + a_2 t + a_3 t^2$$
 (49)

where a_1 , a_2 and a_3 are constants determined by the regression

was found to provide a good fit to the data. Differentiating Equation (49) with respect to t gives the celerity (c) as:

$$c = \frac{dx}{dt} = a_2 + 2a_3t.$$
 (50)

Differentiating Equation (50) gives the acceleration (a_c) of the bro-

$$a_{c} = \frac{d^{2}x}{dt^{2}} = 2a_{3}$$
(51)

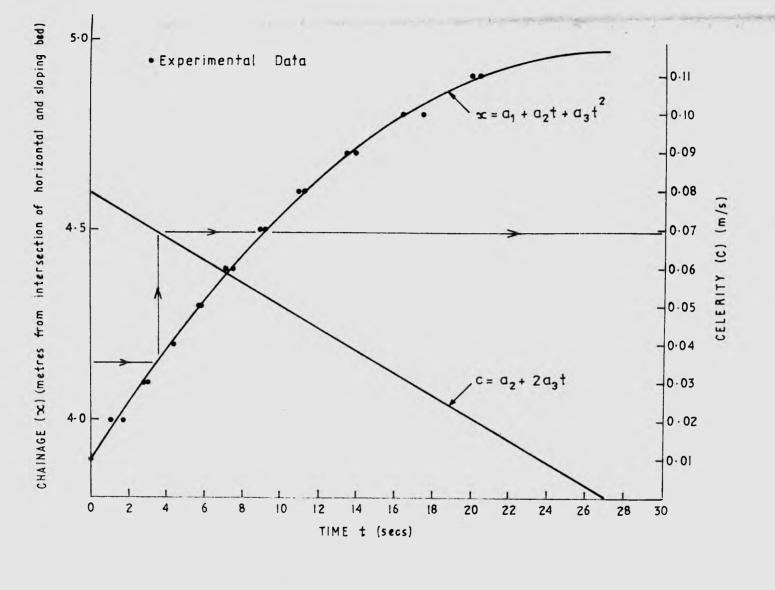
where $a_3 = a$ negative constant.

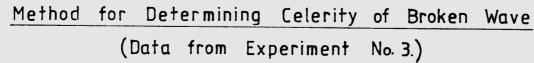
The raw chart recorder trace, x-t plot, and Equations (49) and (50) are shown in Figure (33). Using Figure (33), or its equivalent for the other experiments, it was a simple procedure to select a run-up distance (x_i) , go across to the x-t curve to give the time (t_i) and thence to the t-c curve to give the celerity (c_i) . Chainages (x_i) were chosen to correspond to those for which conductivity (and hence density) profiles were recorded.

5.2.2 Density Excess Measurements

Vertical conductivity profiles were recorded at discrete chainages on the sloping shelf as described in Section (4). To determine the densities within the broken wave and within the backflow it has been assumed that the maximum conductivity correlates to the wave and the minimum conductivity correlates to the backflow. This assumption was supported by visual comparison of the stage of run-up and recorder traces while the experiments were being undertaken. After the maximum and minimum conductivities were extracted from the trace, they were converted to density readings as described in Appendix (3).

The conductivity readings were converted to a density excess $(\rho - \rho_0)$ and normalised with respect to the density excess $(\rho_{\ell} - \rho_0)$ of the lower layer of fluid in the horizontal section of the flume. The density





2.25

excesses $(\rho - \rho_0)/(\rho_l - \rho_0)$ for each chainage were then plotted at the level at which they were recorded (Figure 34) to give the maximum density profile which corresponded to the crest and the minimum which corresponded to the backflow.

The wave height during run-up (H) was defined as the elevation of the 5% density excess level which is shown in Figure (34), a plot of normalised density excess from Experiment No.(2).

The mean density excess (Δ) was defined as:

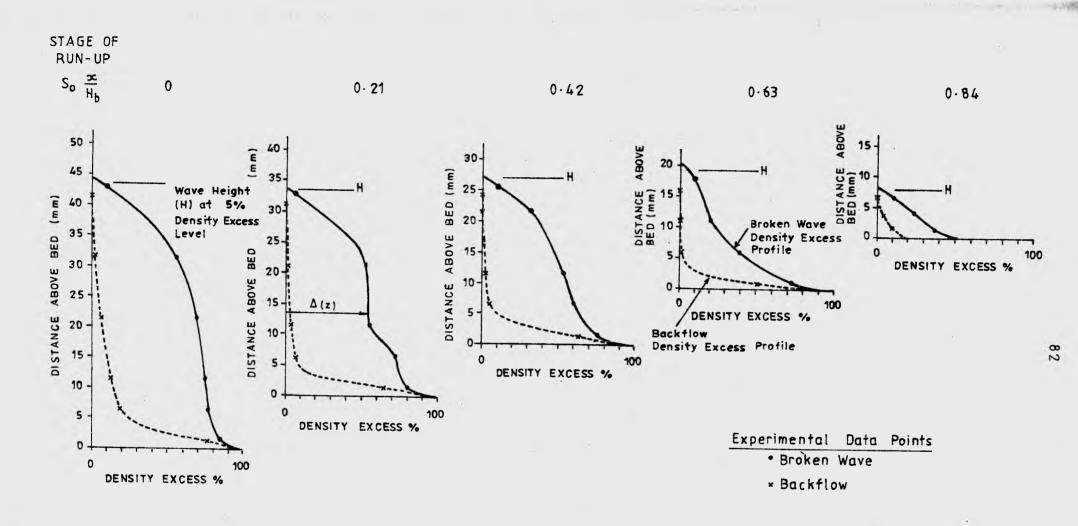
$$\Delta = \frac{1}{H} \int_{z=0}^{H} \Delta(z) \cdot dz$$
 (52)

where $\Delta(z)$ = the vertical distribution of density excess within the broken wave as shown in Figure (34).

5.3 Particle Velocities

As described in Section (4) velocities were determined using neutrally buoyant particles, the resulting data being in one of two forms, either:

- Black and white negatives, each having a bright dot denoting the particle position at the beginning of the exposure and ten to twenty successive fainter dots denoting a pathline for that particle, or
- A series of colour transparencies taken at 1/4 second intervals. Each transparency had one image only of a particle, the particles being different colours for ease of tracking in successive



Normalised Density Excess versus Elevation Above the Bed for Discrete Run-up Chainages (From Experiment No. 2.)

FIGURE 34

slides.

A photographic enlarger was used to analyse the negatives/slides. The advantages over a microfilm reader being:

- The image was brighter than that which could be produced by a microfilm reader.

- The working surface was a horizontal platform as opposed to a vertical screen.

- The surface onto which the image was projected was the one on which the images were traced, that is there was no need to use tracing paper, which was found not to show a clear image when placed on the microfilm reader screen.

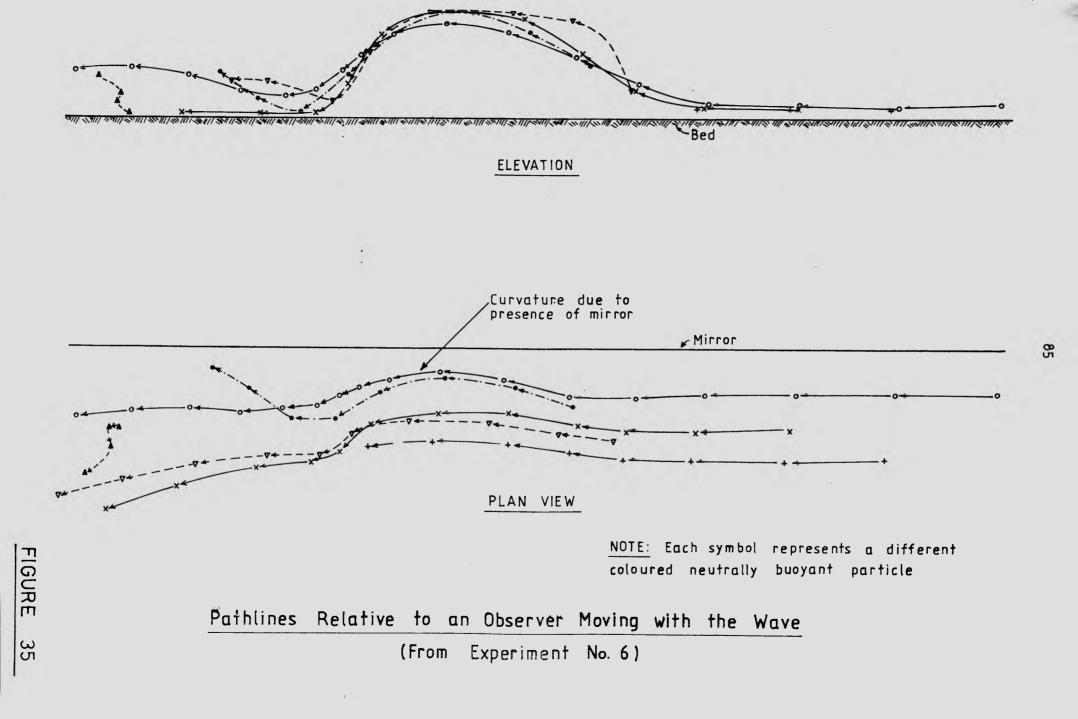
- The image could be set to any size, not being restricted to one or two sizes as in a microfilm reader.

The following summarises the methods used to obtain particle velocity data.

The black and white negatives each showed a series of successive particle locations at 1/4 second intervals. The negatives were enlarged to a convenient scale and the velocities which were proportional to the distances between the particle images were measured directly. The velocities so obtained were relative to a stationary observer. The velocity relative to the wave was calculated as the difference between the particle velocity and the wave celerity at the respective location.

The colour slides were projected onto a sheet of paper and the wave outline, chainage markers and particle locations marked. The particles were marked in their natural colours for ease of identification on successive slides. On successive slides the wave images were superimposed which

resulted in a plot of particle positions relative to an observer moving with the wave. The particle velocities (relative to the wave) were then measured directly. Pathlines were produced by joining successive particle positions as shown in Figure (35).



6.1 Introduction

In this section we describe:

- The experimental results which are the sequel to a series of experiments undertaken by the author as described previously in this thesis, and
- A comparison of the experimental results and the theory which was developed in Section (2).

A summary of the experimental data and parameters is given in Appendix (1). The internal wave characteristics may be divided into two regimes, these being:

- The long wave in the constant depth section of the flume, and
- The shoaling of the wave on the sloping shelf.

6.2 Celerity in Constant Depth Section of the Flume

The celerity of a long, progressive internal wave propagating between rigid boundaries has been given by Equation (11) as:

$$c_{1} = \left[\frac{g_{1}'d_{u}d_{\lambda}}{d_{u}+d_{\lambda}}\right]^{1/2}$$
(11)

Equation (11) represents a simple long wave model which does not take account of the jet like layer observed at the interface during the experiments. The jet like layer is produced by the backflow (from the breaking waves) propagating toward the wave maker along the interface, balancing the (small) mass transport under wave action towards the sloping shelf. Examination of Figure (36), a plot of wave celerity in the constant depth section of the flume reveals that, although Equation (11) is in close agreement with the experimental data, the measured celerities are consistently less than those predicted by Equation (11). It is expected that this discrepancy may be partially accounted for by the retarding effect of the backflow from the breaking waves. This intrusion of the backflow along the interface also results in an increase in the depth of the halocline as mixed fluid is added to the halocline.

6.3 Shoaling of the Wave on the Sloping Shelf

6.3.1 Evaluation of Breaker Height Index

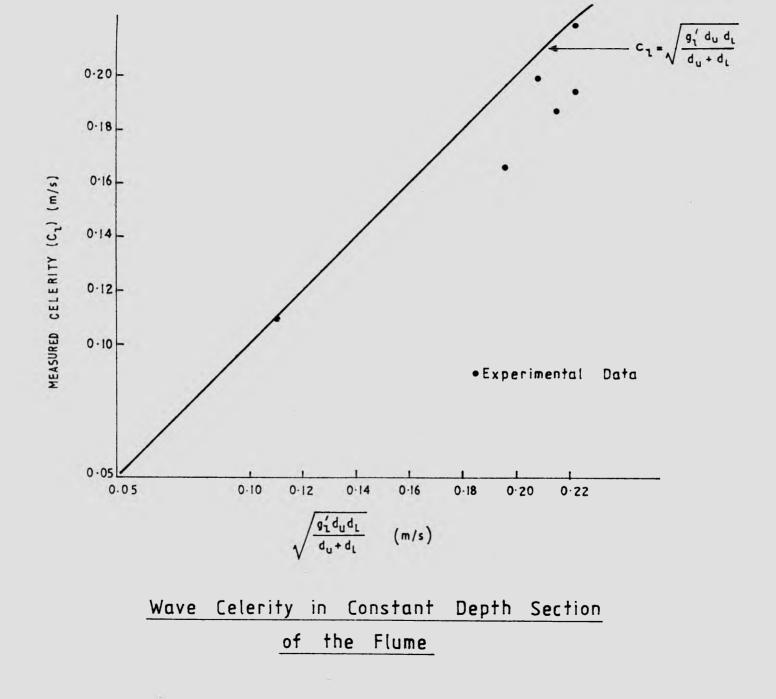
The breaker height index $(H_{h}/H_{)}$ has been given in Equation (27) as:

$$\frac{H_{b}}{H_{l}} = \frac{1}{K_{b}(H_{l}/\lambda_{l})^{1/3}}$$
(27)

where K_{b} was defined in Equation (28) as:

$$K_{b} = \left\{8S_{1} \frac{g_{b}'}{g_{1}'} \left[\frac{(1+C_{v})\mathbb{F}_{b}^{2}}{2} + \chi\right]\right\}^{1/3}$$
(28)

Experimental values of S_0 , g_b'/g_1' , IF_b and K_b which were evaluated in Appendix (4) are given in Table (3).



88

FIGURE 36.

Exp. No.	s _o	g _b ′/g _l ′	₽b	к _b
1	0.030	0.46	0.91	2.15
2	0.030	0.63	0.81	2.28
3	0.030	0.63	0.77	2.24
4	0.030	0.51	0.88	2.20
5	0.030	0.75	0.82	2.43
6	0.054	0.43	0.64	1.85

TABLE 3. Experimental Values of S_0 , g_b'/g_1' , F_b and K_b

As shown in Table (3), experiments give a range of values for K_b from 2.15 to 2.43 (mean of 2.26) for a bedslope of 0.030 and a value of K_b equal to 1.85 for the experiment using a bedslope of 0.054. Equation (27) which has been plotted with values for K_b of 2.26 and 1.85 in Figure (37) represents the analytical breaker height indices for bedslopes of 0.030 and 0.054 respectively.

The experimental breaker height indices (H_b/H_1) have been calculated from the experimental parameters which are tabulated in Appendix (1). Examination of Figure (37), a plot of breaker height indices reveals that the measured values lie close and almost parallel to the analytical solution of Equation (27). However, Equation (27) does consistently underestimate the measured values. Factors which may account for this discrepancy are discussed in the following.

The heights of the breaking waves were measured after the experiment had been running for some time and hence had reached a state of quasiequilibrium where the mass transport upslope in the breaking zone was balanced by the mass transport downslope in the backflow. It was not possible

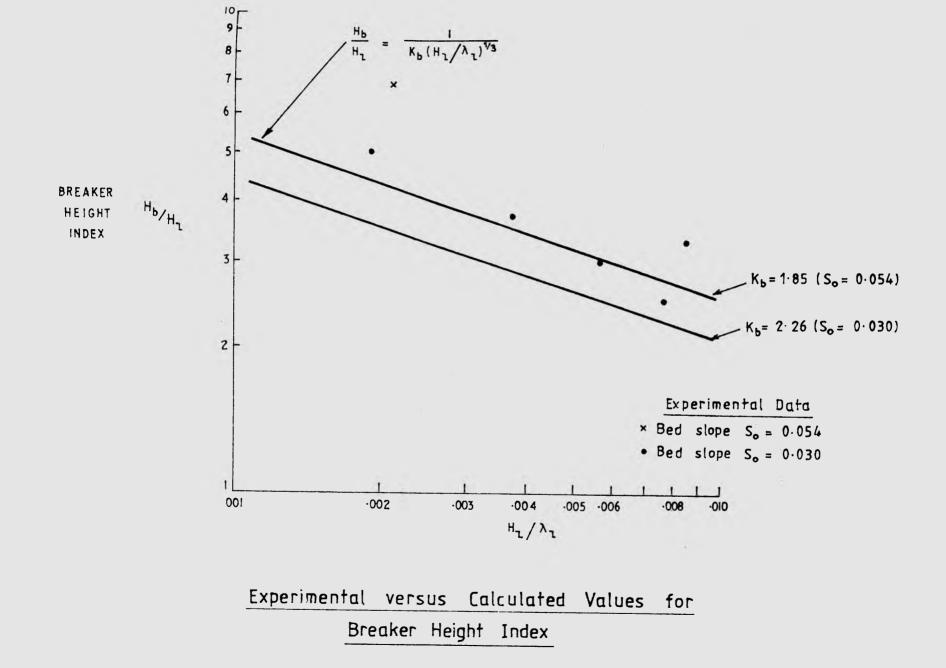


FIGURE 37.

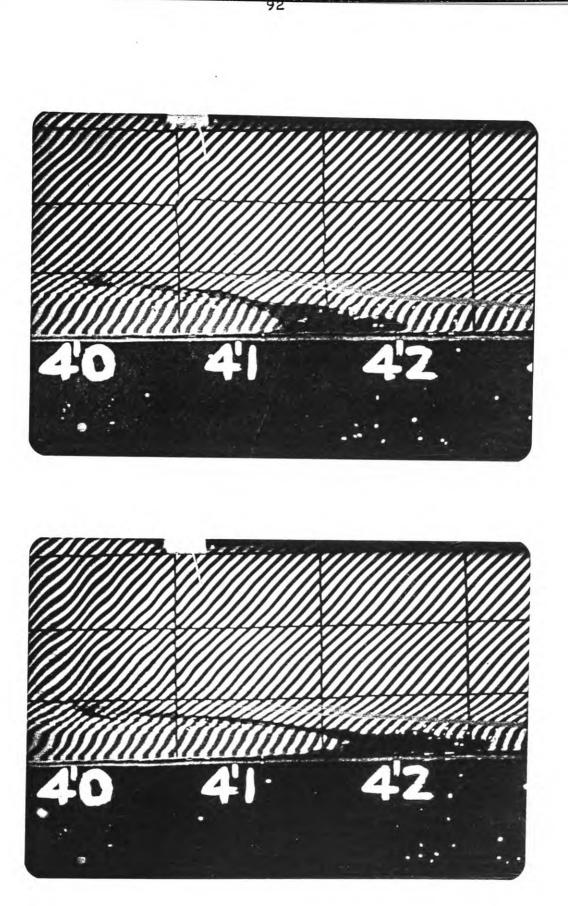
to measure the breaking wave height before this duration as the time which was physically required to measure the relevant parameters was of the order of 20-30 wave periods. Hence it was not possible to collect quantitative data on the first few breaking waves.

Figure (38) shows the first few breaking waves which resemble "class 2" breaking (Figure 7) in which the wave feels no great effect from the shoaling bottom, apart from an increase in the level of the isopycnals above that in the constant depth section of the flume.

It has been qualitatively observed by the author that the wave height at breaking (and hence during run-up) increases significantly after the first few waves. Compare the breaking waves shown in Figure (38) to those which were shown in Figure (11). The waves in Figure (11) indicated that after the breaking process had stabilized the break was more representative of internal surf (in which a discrete bolus of denser fluid runs up the slope) than the "class 2" breaking which described the first few waves as shown in Figure (38).

It is therefore expected that the backflow which is produced by the first few breaking waves may effect the breaking process by:

- Initialising the instability on the forward face of the wave as was shown in Figure (11) which leads to an "internal surf" type of break.
- Causing subsequent waves to break further downslope than the first few waves.



First Few Breaking Waves

The effects of the backflow may also be partially responsible for the breaker height index as predicted by Equation (27) underestimating the experimental breaker height indices as was shown in Figure (37).

It is further proposed that the backflow manifests itself by contributing not only to the wave height at breaking, but also to the wave during run-up. However, during run-up it is the wave as a whole that is of interest, the backflow being a part of this whole.

6.3.2 Evaluation of Run-Up Parameters

6.3.2.1 Wave Height

The height (H) of the broken wave was normalised with respect to the breaking wave height (H_b) for each experiment. The normalised broken wave height (H/H_b) has been given by Equation (43) as:

$$\frac{H}{H_b} = \left[1 - \psi \frac{x}{H_b}\right]$$
(43)

where ψ was defined in Equation (44) as:

$$\psi = \frac{1}{5(1+C_v)} \left[\frac{2S_o}{\mathbb{F}^2} + \frac{C_d}{S_1} \right]$$
(44)

Experimental values of S₀, $\overline{\mathbf{F}}$, ψ and ψ/S_0 which were evaluated in Appendix (4) are given in Table (4) overpage.

As shown in Table (4), for the limited range of bedslopes tested, experiments give the value of ψ to be approximately equal to the bedslope (S₀).

Exp. No.	s _o	ĪF	ψ	ψ/s _o
1	0.030	0.92	0.029	0.97
2	0.030	0.91	0.029	0.97
3	0.030	0.84	0.031	1.03
4	0.030	0 .9 0	0.029	0.97
5	0.030	0.83	0.031	1.03
6	0.054	0.65	0.052	0.96

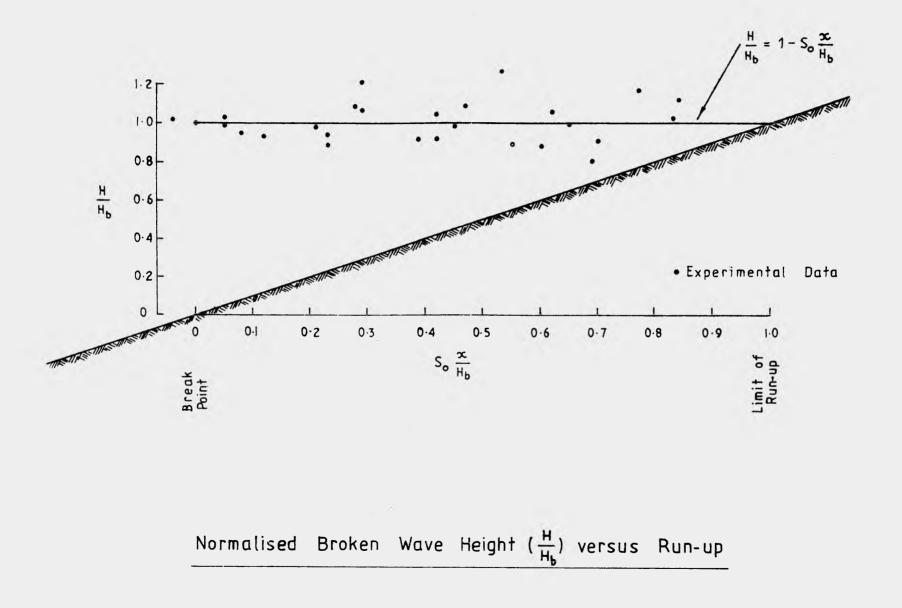
TABLE 4. Experimental Values of S₀, $\overline{\mathbf{F}}$, ψ and ψ/S_0

Substituting S for ψ into Equation (43) gives:

$$\frac{H}{H_b} = \left[1 - S_o \frac{x}{H_b}\right]$$
(53)

The run-up distance (x) was normalised with respect to the wave height at breaking and then multiplied by the bedslope to enable the relationship in Equation (53) to be plotted directly. This also enabled data from experiments with different bedslopes to be superimposed on the one plot, the advantage being that the bedslope could be now taken as any value. However, it must be noted that it is not known if $\psi \approx S_0$, and hence if Equation (53) applies for bedslopes outside the range of those used in this study.

Examination of Figure (39), a plot of wave height versus stage of run-up reveals that Equation (53) represents a horizontal line, irrespective of bedslope. The experimental data shows good agreement, the crest elevation of the wave remaining approximately constant during run-up. A least squares linear regression applied to the data which is plotted in Figure (39) yields;



$$\frac{H}{H_{b}} = 0.96 \left[1 - S_{0} \frac{x}{H_{b}}\right]^{0.93}$$
(54)

with a correlation coefficient (R) of 0.87. Comparison of Equations (53) and (54) shows that the experimental data closely approximates the analytical solution, the regression wave height being proportional to $x^{0.93}$ as opposed to $x^{1.00}$ as derived in the analytical solution.

6.3.2.2 Wave Celerity

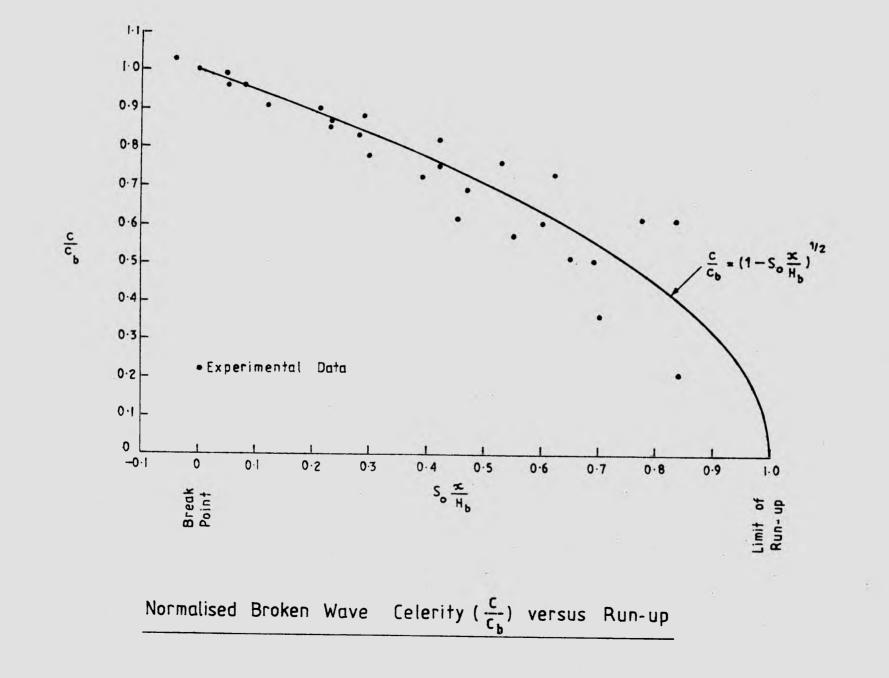
Having determined that $\psi \simeq S_{\phi}$, Equation (46) can now be written as:

$$\frac{c}{c_b} = [1 - S_o \frac{x}{H_b}]^{1/2}$$
(55)

Equation (55) relates the celerity of a broken internal wave normalised with respect to the wave celerity at breaking (c_b) to the stage of run-up. Figure (40), a plot of wave celerity versus run-up shows that the celerity diminishes as the wave progresses up the slope. The experimental data is a good fit to Equation (55) in the early stages of run-up, although the deviation does increase with run-up. A least squares power curve regression applied to the experimental data gives:

$$\frac{c}{c_b} = 1.00 \left[1 - S_0 \frac{x}{H_b}\right]^{0.56}$$
(56)

with a correlation coefficient (R) of 0.85. Equation (56) shows good agreement with the theoretical relationship which was derived in Equation (55). The measured celerities are proportional to $x^{0.56}$, a slight deviation from the predicted value of $x^{1/2}$.



.97

FIGURE 40.

6.3.2.3 Density Excess

It was assumed in Section (2) that the variation in density excess within the wave during run-up was proportional to x^e , and subsequently that if the system was two layered with no mixing then (e) was equal to zero. The validity of the no mixing assumption will now be evaluated.

If the two layers were immiscible, then the assumption would be valid. By contrast, at the interface between miscible fluids, mixing by entrainment and diffusion can almost be accepted as a universal process. This results in a variation both in density and hence Δ and g' in miscible fluids.

Figure (41) shows a plot of the mean density excess of fluid contained within the wave $(\rho - \rho_u)$ normalised with respect to the mean density excess within the wave at breaking $(\rho_b - \rho_u)$ for the wave running up a gently sloping shelf. Note that $(\rho - \rho_u)/(\rho_b - \rho_u)$ is equal to g'/g_b' .

Experiments indicate that the mean density excess within the wave decreases during run-up, this being the result of entrainment of less dense overlying fluid. This is accompanied by drainage from the leeward side of the wave as was shown in Figure (10).

If it is assumed that the density excess within the wave tends to zero at the limit of run-up and is proportional to x^e as noted above then the variation in the density and hence effective gravitational acceleration during run-up can be approximated by a power curve, as indicated by experiments, of the form:

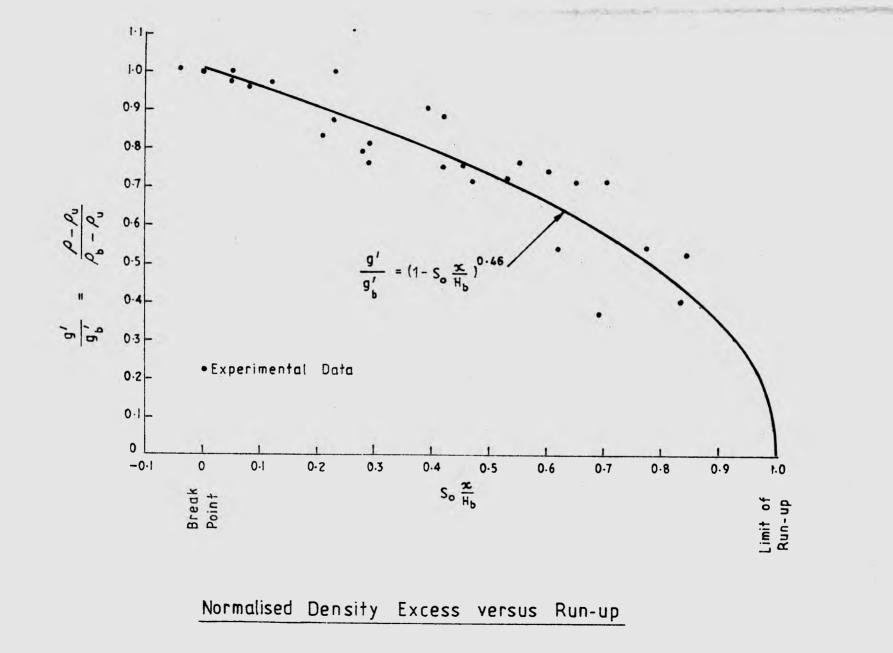


FIGURE 41.

$$\frac{g'}{g_{b}'} = \Gamma[1 - S_{oH_{b}}^{x}]^{e}$$
(57)

Where Γ , e = dimensionless constants

A least squares power regression analysis of Equation (57) gives values for Γ and e of 0.99 and 0.46 respectively, and a correlation coefficient (R) of 0.85. Equation (57) can therefore be approximated by Equation (58) which has been plotted on the experimental data in Figure (41).

$$\frac{g'}{g_b'} = \left[1 - S_o \frac{x}{H_b}\right]^{0.46}$$
(58)

6.3.3 Validity of the Similarity Solution

In Section (2) it was assumed that a similarity solution existed such that $c \propto x^a$, $H \propto x^b$, g' $\propto x^e$ and a Froude number which was defined in Equation (39) as:

$$\mathbf{F} = c/(g'H)^{1/2}$$
(39)

was constant during run-up.

Substituting values for a, b and e which were evaluated from the . regression analyses described above gives:

IF
$$\propto x^{a-(b/2)-(e/2)}$$

= $x^{-0.14}$

which is close to the value of x^0 which was derived from the similarity analysis. A plot of Froude number versus run-up which is shown in Figure

(42) shows no significant variation in Froude number with run-up. The similarity solution as derived in Section (2) is therefore considered to be justified.

Note that the Froude numbers for the last 25% of the run-up distance were excluded from Figure (42) as they gave an unreasonable scatter of results. These data will be discussed later in this section.

6.3.4 Particle Velocities

Particle velocities in the model were measured by tracking neutrally buoyant particles as described in Section (3). The maximum (~ horizontal) particle velocities (u) from each frame of film (or between successive frames as applicable) were extracted, and normalised with respect to the wave celerity at breaking. The normalised particle velocities are plotted in Figure (43) at their respective locations ($S_o x/H_b$) from the breakpoint.

The apparent wide scatter of maximum recorded particle velocities for a given distance from the breakpoint is a result of the transient nature of the velocities with the maximum velocity, at any given location, being achieved for only a fraction of the wave period as the broken wave passes that location. Hence the maximum velocities recorded depended very much upon having a particle to track in the right place at the right time. The maximum velocities should therefore be taken as the envelope of recorded velocities as shown by a dashed line in Figure (43). Examination of Figure (43) reveals that:

• Maximum particle velocities exceed the wave celerity by up to $\sim 50\%$ just after breaking.

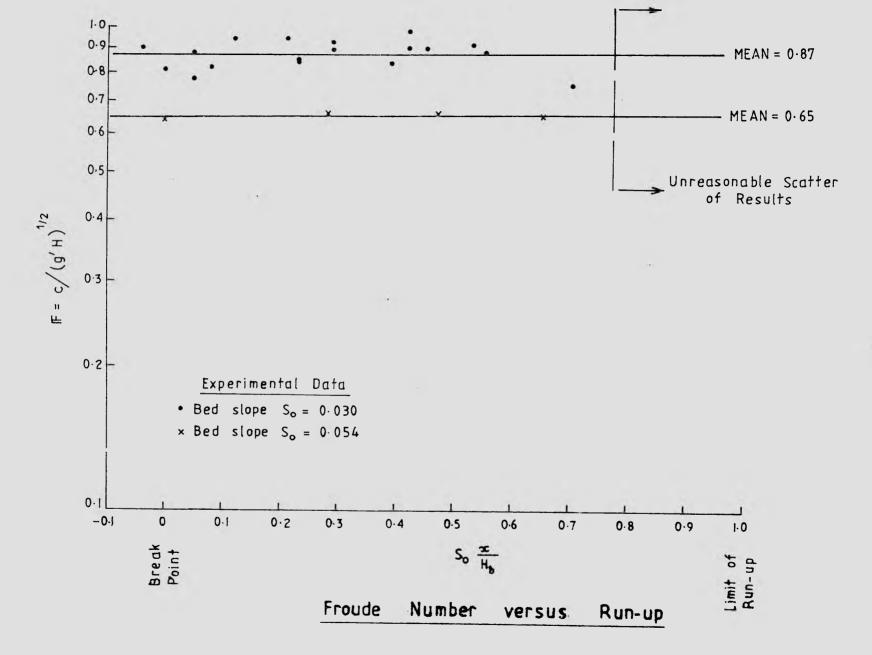


FIGURE 42

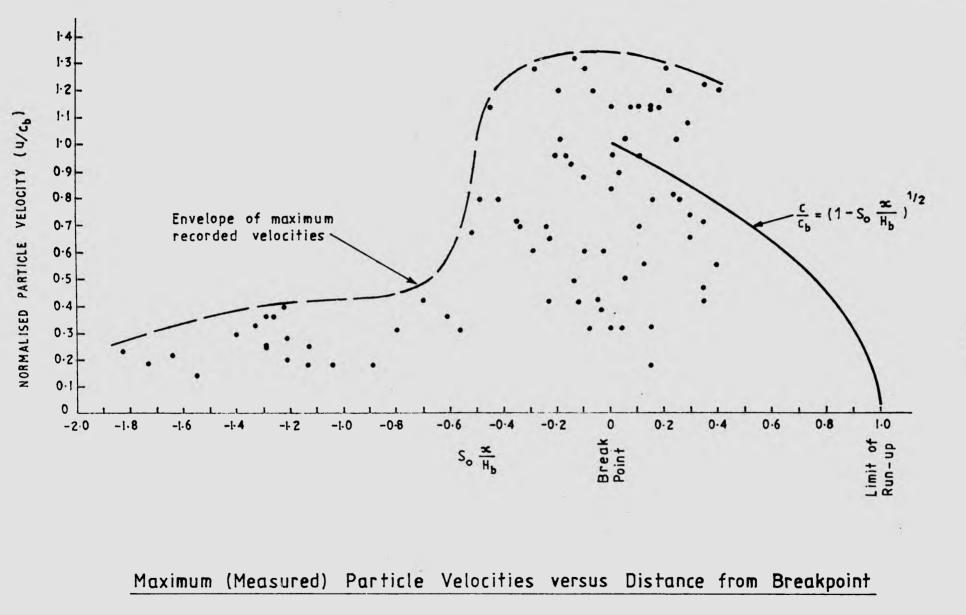


FIGURE 43.

- Maximum particle velocities just prior to breaking $(S_0 x/H_b \sim -0.4 \text{ to } 0)$ approximately equal those just after breaking $(S_0 x/H_b \sim 0 \text{ to } 0.4)$. The magnitude of these velocities is ~ 30% greater than the celerity at breaking (c_b) , and occurs over a total range of ~ 70% of the run-up distance, a significant distance if prototype shelf slopes and breaking conditions are considered (Appendix 6).
- In regions far before the breakpoint $(S_0 x/H_b \sim -2)$ maximum particle velocities are an order of magnitude less than the wave celerity, noting that the wave celerity at breaking is ~ 1/2 of the wave celerity in the constant depth section of the flume.
- At breaking particle velocities have increased by an order of magnitude over particle velocities far downslope of the breaking region.

Note that reversals of direction of particle velocities have also been recorded. Referring back to Figure (28), the pathlines denoted by the neutrally buoyant particles clearly indicate reversals of direction. This is a result of the flow pattern that describes a broken internal wave as it passed a fixed reference point. As the wave passes the reference point high upslope velocities are generated near the bed, thence to quickly reduce to zero and reverse as the drainage from the wave accelerates downslope. The downslope velocities near the bed revert to upslope velocities during the passage of the next wave and the process repeats. This velocity pattern is similar to that observed by Cresswell (1974, Figure 5), if it is assumed that Cresswell's readings include a tidal current component.

6.4 Scale Effects

As noted in Section (1), scale effects in the model were minimised by ensuring that model Reynolds numbers were as large as possible. This was achieved by exaggerating the density difference between the layers using a halocline with $(\rho_{\ell} - \rho_{u})/\bar{\rho} \sim 0.04$ to simulate the ocean thermocline where $(\rho_{\ell} - \rho_{u})/\bar{\rho} \sim 0.0004$.

The Reynolds number, which is a measure of the ratio of the dynamic forces to the viscous forces in the flow was given in Equation (3) as:

$$IR = \frac{cH}{v}$$
(3)

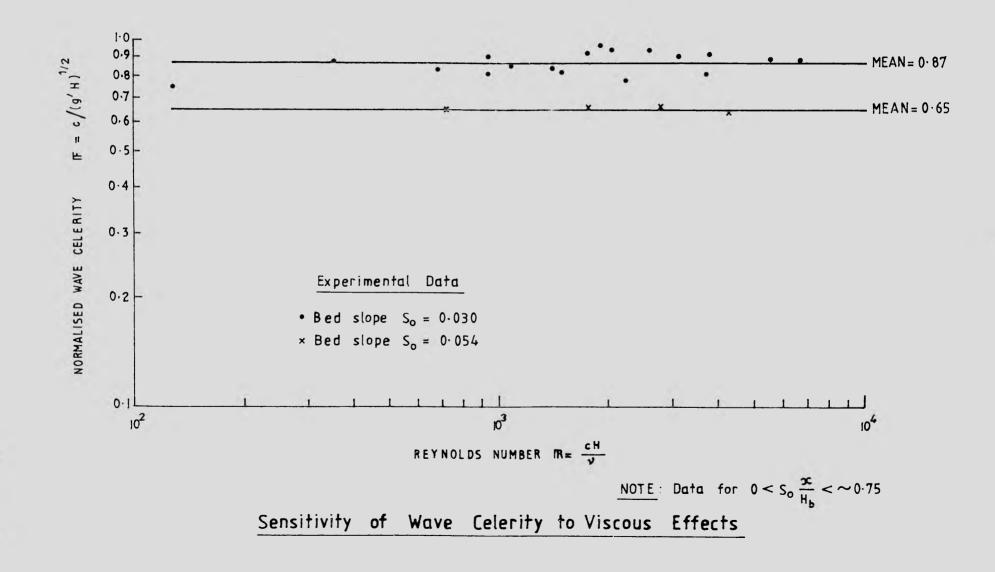
The celerity of a long internal wave is given by:

$$c = \left[\frac{\rho_{\chi} - \rho_{u}}{\rho_{u}} g d_{u}\right]^{1/2} \approx \left[\frac{d_{u}}{d_{\chi}}\right]$$
(59)

where Ω = a function of d_{μ}/d_{ρ}

It can be seen through Equation (59) that for the given increase in density difference, the wave celerity and hence Reynolds numbers were thereby increased by an order of magnitude.

As shown in Figure (44), for the range of Reynolds numbers applicable to the first 75% of run-up, the normalised wave celerity $c/(g'H)^{1/2}$ was found to be independent of Reynolds number. Viscous effects were therefore not important in this range of the experiments and it is expected that the model results are representative of the prototype.



106

.

However, near the limit of run-up ($S_0 x/H_b > ~75\%$), the magnitudes of the wave height and celerity were reduced to a scale where viscous effects and the relative errors in measurement were significant. The compounding of errors which results from the calculation of a Froude number leads to a totally unreasonable scatter of values and hence the Froude number has been disgarded for values of $S_0 x/H_b > ~75\%$.

However, individual wave height, celerity and density excess measurements still gave meaningful results for run-up values $(S_0 x/H_b)$ up to ~85%, and hence are included in the data plots up to this limit.

7. LIST OF REFERENCES

- Alonso, C.V. (1971). Comparative study of electrical conductivity probes. J. Hyd. Res, 9, No. 1, pp 1-10.
- [2] Benjamin, T.B. (1968). Gravity currents and related phenomena. J.Fluid Mech. Vol. 31, Pt 2, pp. 209-248.
- [3] Cacchione, D.A. (1970). Experimental study of internal gravity waves over a slope. Mass. Inst. Technol., Dept. Earth and Planetary Sciences, Report 70-6, 226 pp.
- [4] Cairns, J.L. and LaFond, E.C. (1966). Periodic motions of the seasonal thermocline along the southern California coast, J. Geophys. Res. 71 (16), pp. 3903-3915.
- [5] Cresswell, G.R. (1974). Ocean currents measured concurrently on and off the Sydney area continental shelf. Aust. J. Mar. Freshwat. Res., 25, pp. 427-38.
- [6] Defant, A. (1961). Physical oceanography, Vol. II. London: Pergamon Press.
- [7] Emery, K.O. and Gunnerson, C.G. (1973). Internal swash and surf.
 Proc. Nat. Acad. Sci. USA, <u>70</u>, No. 8, pp. 2379-2380.
- [8] Goda, Y. (1970). A synthesis of breaker indices, Transactions of the Japanese Society of Civil Engineers, Vol. 2, Part 2.

- [9] Görtler, H. (1943). Uber eine Schwingungserscheingung in Flüssigkeiten mit stabiler Dichteschichtung. Z. agnew. Math. Mech. 23, 65-71.
- [10] Hall, J.M. and Pao, Y-H (1969). Spectra of internal waves and turbulence in stratified fluids. Radio Science, <u>4</u>, No. 12, pp. 1321-1325.
- [11] Lamb, H. (1952). Hydrodynamics, Sixth Edition (Reprinted), Cambridge University Press, New York.
- [12] Mowbray, D.E. and Rarity, B.S.H. (1967). A theoretical and experimental investigation of the phase configuration of internal waves of small amplitude in a density stratified liquid. J. Fluid. Mech. Vol. 28, pp. 1-16.
- [13] Munk, W.H. (1949). The solitary wave theory and its application to surf problems, Annals of the New York Academy of Sciences, Vol. 51, pp. 376-462.
- [14] Murota, A., Hirata, T. and Michioku, K. (1981). Characteristics of internal gravity wave and its breaking on sloping bed. Trans. Japan Soc. Civ. Eng., Hyd. and Sanitary Eng. Div. <u>12</u>, pp. 149-150.
- [15] Nagashima, H. (1971). Reflection and breaking of internal waves on a sloping beach. J. Ocean. Soc. Japan, 27, pp. 1-6.
- [16] Oil and Gas Journal (1979). "Hostile-environment technology advances for deep water, Arctic." Tulsa, Okla. Sept, 1979, pp 66-68.

- [17] Osborne, A.R. and Burch, T.L. (Undated), Internal Solitons in the Andaman Sea. Unpublished Draft, International School of Physics, "Enrico Fermi", Varenna.
- [18] Patrick, D.A. and Wiegel, R.L. (1955). Amphibian tractors in the surf, Proc. First Conf. on Ships and Waves, Council on Wave Research and Society of Naval Architects and Marine Engineers, pp. 397-422.
- [19] Roberts, J. (1975). Internal gravity waves in the ocean. Marcel Dekker, Inc., New York.
- [20] Robertson, J.M. (1965). Hydrodynamics in theory and application, Prentice-Hall, Inc., Englewood Cliffs. N.J.
- [21] Southard, J.B. and Cacchione, D.A. (1972). Experiments on bottom sediment movement by breaking internal waves. Chapter 4 in "Shelf Sediment Transport: Process and Pattern". Ed. by D.J.P. Swift, D.B. Duane and D.H. Pilkey. Stroudsburg, Pennsylvania, Dowden, Hutchinson and Ross, 1972.
- [22] Tuma, J.J. (1979). Engineering Mathematics Handbook. McGraw-Hill, Inc. New York.
- [23] Turner, J.S. (1979). Buoyancy effects in fluids. Cambridge: Cambridge University Press.
- [24] Wilkinson, D.L. and Wood, I.R. (1972). Some observations on the motion of the head of a density current. J. Hydr. Res., <u>10</u>, No. 3, pp. 305-324.

APPENDIX 1

<u>A</u> <u>SUMMARY</u> OF <u>EXPERIMENTAL</u> <u>DATA</u> <u>AND</u> <u>PARAMETERS</u>

TABLE 5. WAVE CHARACTERISTICS IN THE CONSTANT DEPTH SECTION OF THE FLUME

Exp.No.	d 1	d _u	H ₁	Т	с	λ _ι	Η _ι /λι	۵.
	mm	mm	mm	S	ms ⁻¹	m		
1	125	375	7.2	18.9	0.198	3.76	0.0019	0.0465
2	125	375	11.5	18.9	0.165	3.11	0.0037	0.0413
3	130	370	9.8	6.33	0.186	1.16	0.0084	0.0484
4	130	37 0	20.6	18.9	0.193	3.65	0.0056	0.0514
5	130	370	15.5	18.8	0.109	2.05	0.0076	0.0129
- 6	135	.365	8.4	18.8	0.218	4.09	0.0021	0.0506

Exp.No.	н _ь	с _b	∆ _b	н _ь /н	c _b /cı	۵ _b /۵	So	IF _b	× _b
	mm	ms ⁻¹							
1	36	0.079	0.0214	5.0	0.40	0.46	0.030	0.91	3.85
2	43	0.085	0.0260	3.7	0.51	0.63	0.030	0.81	4.00
3	32	0.077	0.0305	3.3	0.41	0.63	0.030	0.77	3 .9 5
4	62	0.109	0.0262	3.0	0.56	0.51	0.030	0.88	4.20
5	38	0.047	0.0097	2.5	0.43	0.75	0.030	0.82	3.90
6	58	0.071	0.0220	6.9	0.33	0.43	0.054	0.64	2.80

TABLE 6. WAVE CHARACTERISTICS AT BREAKING

Exp No	×c	x	s _{oHb}	Н	н/н _b	с	c/c _b	g'H	g ʻ	g' g _b '	IF	R	h	L	H/L
 	m	m		m		ms ⁻¹		m ² s ⁻²	ms ⁻¹				m	m	
1	3.80	05	04	.038	1.06	.081	1.03	.00811	.213	1.02	.9 0	3080	.014	.112	•34
	4.00	•15	•12	.029	.81	•072	•91	.00592	•204	.97	•94	209 0	•008	.091	.32
	4.20	• 35	•29	•028	•78	•062	.78	.00447	.160	.76	•92	1740	.005	.122	.23
	4.40	• 55	•45	.019	•53	.049	•62	.00301	.158	.75	•9 0	930	.007	.083	•23
2	4.00	•00	•00	.043	1.00	.085	1.00	•010 9 0	•253	1.00	.81	3660	.015	.130	.33
	4.30	•30	•21	.033	.77	.078	.92	.00688	.208	•82	•94	2570	.006	.103	.32
	4.60	•60	•42	.027	•63	.070	.82	.00518	.192	•75	.97	18 9 0	.005	.082	.33
	4.9()	. 90	•62	.019	.44	.062	.73	.00259	•136	•54	1.22	1180	•006	.061	.31
	5.20	1.20	.83	•008	.19	.052	•61	.00081	.101	•40	1.83	42 0	•002	.026	.31

113

.

Exp No	×c	x	s x oH _b	н	н/н _ь	с	c/c _b	gʻH	g'	g' gb	F	IR	h	L	H/L
	m	m		m		ms ⁻¹		m ² s ⁻²	ms-1				m	m	
3	4.00	•05	•05	•030	•94	•074	•96	•0089 2	•297	•99	•78	2220	-	•097	.31
	4.20	•25	•23	.021	•66	•067	.87	.00626	•298	•99	•84	1410	-	•084	•25
	4.40	•45	•42	•016	•50	•058	•75	•0041 7	•261	•87	•9 0	930	•00 6	•0 73	.22
	4.60	•65	•60	•00 9	•28	•046	•60	.00199	•221	•74	1.03	410	-	-	-
	4.70	•75	•69	•004	•13	•039	•51	.00038	•095	•32	2.00	140	-	-	-
4	4.30	.10	•05	•061	•98	.108	•99	•01500	•246	•96	•88	659 0	•023	.156	•39
	4.80	•60	•29	•057	•92	•096	•88	•01170	•205	•80	.89	5470	•014	.197	.29
	5.30	1.10	•53	.045	•73	•083	•76	•00826	•184	•72	•91	3740	.005	-	-
	5.80	1.60	•77	•024	•39	•067	•61	•00332	.138	•54	1.16	1610	•00 3	-	-

TABLE 7. SUMMARY OF EXPERIMENTAL PARAMETERS DURING RUN-UP (CONTINUED)

TABLE 7. SUMMARY OF EXPERIMENTAL PARAMETERS DURING RUN-UP (CONTINUED)

			<u> </u>								1				
xp Io	×c	x	son x	н	н∕ н _ь	с	c/c _b	g'H	gʻ	g' gb	ŀ	R	h	L	H/ 1
	m	m		m		ms ⁻¹		m ² s ⁻²	ms ⁻¹				m	m	
5	4.00	•10	•08	.033	.87	•045	•96	•00298	•090	.95	•82	1490	•008	.106	.3
	4.20	•30	•23	•027	•71	•040	•85	•00222	.082	.87	•85	1080	.007	.096	•28
	4.40	•50	•39	.020	•53	•034	•72	.00169	.085	•89	.83	680	•006	.083	•24
	4.60	• 7 0.	•55	.013	-34	.027	•57	•00094	.072	•76	.88	350	.004	.057	•23
	4.80	•9 0	•70	•008	•21	.017	•36	.00051	.064	.67	•75	130	-	-	-
6	2.80	•00	•00	•058	1.00	.071	1.00	•01250	. 216	1.00	•64	4250	.009	•252	•23
	3.10	•30	•28	•047	.81	•059	•83	• 00 803	.171	.79	•66	2770	.008	.142	.33
	3.30	•50	•47	.036	•62	•049	•69	•00545	•151	.7 0	.66	1760	•004	-	-
	3.50	•70	•65	•020	•34	•036	•51	•00307	•154	.71	.65	72 0	.003	.053	.3
	3.70	• 9 0	•84	•016	•28	•015	•21	.00179	•120	•52	•35	240	•00 2	.047	•34

Exp.No.	×c	x	Sox/H	u	
4 44 ⁻¹ 14 4	m	m		ms ⁻¹	
1	2.30	-ì.55	-1.29	•020	
5. 	2.30	-1.55	-1.29	.019	
	2.40	-1.45	-1.21	•022	
	2.40	-1.45	-1.21	.016	
	2.50	-1.35	-1.13	.020	
	2.50	-1.35	-1.13	•014	
	2.60	-1.25	-1.04	•014	
	3.75	-0.10	-0.08	.025	
	3.80	-0.05	-0.04	•030	
	3.85	0.00	0.00	•025	
	3.90	0.05	0.04	•025	
2	2.00	-2.00	-1.40	.025	
	2.10	-1.90	-1.33	•027	
,	2.15	-1.85	-1.29	.031	
	2.20	-1.80	-1.26	.031	
	2.25	-1.75	-1,22	.034	
	3.20	-0.80	-0.56	•026	
1	3.25	-0.75	-0.52	•057	
	3.30	-0.70	-0.49	•067	
	3.35	-0.65	-0.45	•096	
	3.40	-0.60	-0.42	•067	
	3.50	-0.50	-0.35	.060	
	3.70	-0.30	-0.21	.081	
	3.75	-0.25	-0.17	.081	
	3.80	-0.20	-0.14	.111	

.

TABLE 8. MAXIMUM (MEASURED) PARTICLE VELOCITIES

xp.No.	×c	x	Sox/H	u	u/c _b
-	m	m		ms ⁻¹	
2	3.85	-0.15	-0.10	.051	0.60
	3.90	-0.10	-0.07	.101	1.19
	3.95	-0.05	-0.03	.051	0.60
	4.00	0.00	0.00	•096	1.13
	4.05	0.05	0.03	.076	0.89
	4.10	0.10	0.07	.096	1.13
	4.15	0.15	0.10	.096	1.13
	4.20	0.20	0.14	•0 9 6	1.13
	4.25	0.25	0.17	•096	1.13
	4.30	0.30	0.21	.101	1.19
	4.35	0.35	0.24	.085	1.01
	4.40	0.40	0.28	•091	1.07
3	2.00	-1.95	-1.83	.018	0.23
	2.10	-1.85	-1.73	.014	0.18
	2.20	-1.75	-1.64	.016	0.21
	2.30	-1.65	-1.55	.011	0.14
	3.00	-0.95	-0.89	.014	0.18
	3.10	-0.85	-0.80	•024	0.3
	3.20	-0.75	-0.70	.032	0.42
	3.30	-0.65	-0.61	•0 28	0.36
	3.70	-0.25	-0.23	•050	0.6
	3.70	-0.25	-0.23	•032	0.4
	3.80	-0.15	-0.14	•038	0.49
	3.90	-0.05	-0.05	.032	0.4
	4.00	0.05	0.05	.078	1.0
	4.10	0.15	0.14	.086	1.1
	4.20	0.25	0.23	.062	0.8

TABLE 8. MAXIMUM (MEASURED) PARTICLE VELOCITIES (CONTINUED)

	r					
	Exp.No.	× c	x	Sox/H	u	u/c b
-		m	m		ms ⁻¹	
		,				
	4	3.50	-0.70	-0.34	.075	0.69
		3.60	-0.60	-0.29	•065	0.60
		3.70	-0.50	-0.24	•075	0.69
		3.80	-0.40	-0.19	.110	1.01
		3.90	-0.30	-0.15	.100	0.92
		3.95	-0.25	-0.12	.045	0.41
		4.00	-0.20	-0.10	•095	0.87
		4.20	0.00	0.00	•0 9 0	0.83
		4.30	0.10	0.05	•055	0.50
		4.40	0.20	0.10	.075	0.69
· .		4.45	0.25	0.12	.060	0.55
		4.50	0.30	0.15	•032	0.32
		4.50	0.30	0.15	•020	0.18
		4.80	0.60	0.29	.080	0.73
		4.90	0.70	0.34	•050	0.46
		4.90	0.70	0.34	.045	0.41
	- 8 - 1	5.00	0.80	0.39	.130	1.19
		5.00	0.80	0.39	.060	0.55
4. 1		•				
	6	2.50	-0.30	-0.29	•0 9 0	1.27
		2.60	-0.20	-0.20	•084	1.19
		2.70	-0.10	-0.10	•090	1.27
		2.8 0	0.00	0.00	•067	0 .9 5
	-	2.90	0.10	0.10	.067	0.95
		2.95	0.15	0.15	•056	0.79
-		3.00	0.20	0.20	•090	1.27
		3.05	0.25	0.24	•056	0.79
		3.10	0.30	0.28	.046	0.65
		3.15	0.35	0.33	.071	1.2
1	(i)	3.15	0.35	0.33	•050	0.71

· · ·

APPENDIX 2

DETAILS OF NEUTRALLY BUOYANT PARTICLES USED FOR VELOCITY MEASUREMENTS

As described in Section (3), particle trajectories and velocities were obtained by recording on film the motion of neutrally buoyant particles. In order to be effective velocity indicators the neutrally buoyant particles had to be:

- Insoluble and non-reactive with fresh water and saline solutions.
- Of densities within the required range and spread so as to adequately cover the densities within the halocline.
- Clearly visible, fairly symmetrical, and plentiful in supply or easily retrievable for use in successive experiments.
- Of dimensions less than that of fine scale turbulence within the flow.
- Small enough so as to closely approximate water particle velocities, that is, the ratio of the drag force on the particle (proportional to length²) to the particle's inertia (proportional to length³) must be high.
- Such that the introduction of the particles into the system would not disturb the flowfield to any significant extent.

The types of particles considered were:

• Sand grains imbedded in wax,

• Liquid hydrocarbon combinations and

• Polystyrene beads.

The first option was rejected as it was extremely difficult to obtain the desired density range during production, which was extremely time consuming as each particle had to be produced individually. Liquid hydrocarbons were also rejected due to their lack of rigidity which allowed them to break up and become emulsified in regions of high turbulence, which would in turn lead to fouling of the conductivity probes.

Polystyrene beads, which were in plentiful supply were chosen for use as neutrally buoyant particles. The beads were white and opaque, ranging in diameter from ~ 0.5 mm to ~ 2.0 mm. Sieving produced a range of beads in size from 1.0 mm to 1.4 mm. The relative density of the beads ranged from ~1.01 to ~1.04 with a good scatter of densities throughout the range. The white beads possessed good reflective properties for the experimental sequences illuminated by multiple flash, while a light spray with fluorescent paint readily coloured the beads for use with colour film.

APPENDIX 3

CONDUCTIVITY PROBES

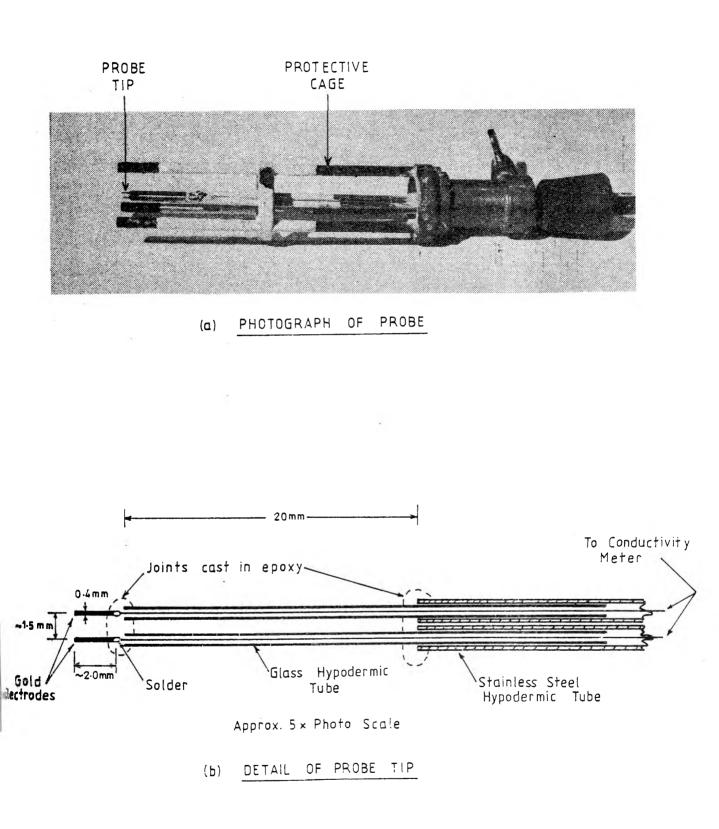
In this section are described the design, construction, platinization, calibration and maintenance of the four conductivity probes which were used in the experiments.

Design and Construction

The selection of the type of probe was based on the following requirements:

- Dimensions to be such that the flow field was not appreciably disturbed by the presence of the probe.
- Probe to be corrosion resistant in salt water.
- Conductivity to vary proportionally to salinity (or density excess).
- Probe to be robust.
- Probe to sample as small a volume as practical.
- Probe to be relatively simple and inexpensive to construct.

The probe, which is based on a design described by Alonso (1971) is shown in Figure (45). The electrodes were made from 0.6 mm diameter gold wire, soldered to connecting leads which pass through and are supported by glass hypodermic tubing which was encased in stainless steel tubing ~ 20 mm



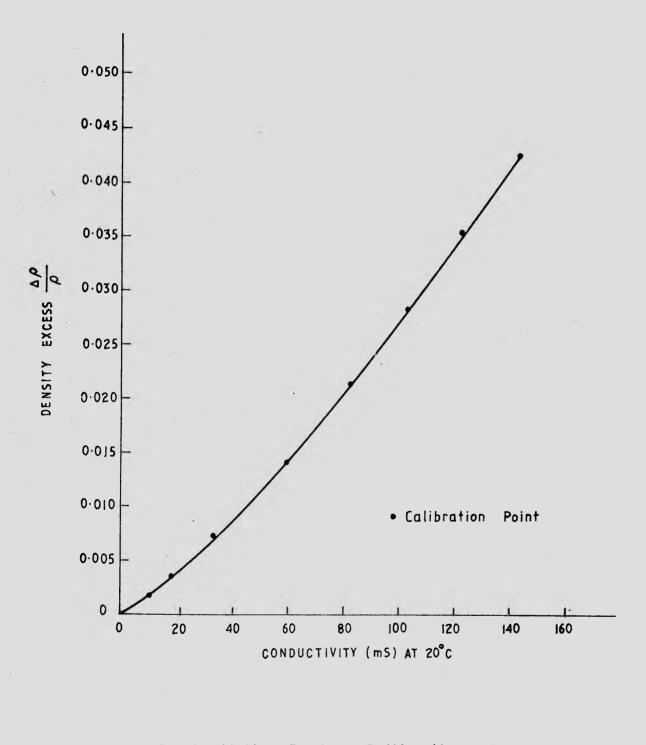
Conductivity Probe

from the electrodes. Glass tubing was used near the electrodes for its insulating properties and stainless steel thereafter for strength. All joints were cast in epoxy resin for corrosion resistance and to prevent water entering the tubes. After platinizing the probes were placed within protective cases as shown in Figure (45) to prevent accidental damage to the fragile tip.

Platinizing, Calibration and Maintenance

The probe electrodes were platinized by the method as described by Cacchione (1970). The main reason for platinizing the electrodes was to increase the linearity of the output at higher conductances, that is for density excesses above ~ 2%. The probes were calibrated in solutions of known salinity (and hence density excess) in a water bath at a constant temperature of 20° C. The calibration curves between probes differed as a result of differences in geometry during construction and the degree of platinization. A typical calibration curve is given in Figure (46). The conductivity readings were converted directly to a density excess reading by use of the calibration curves. The temperature coefficient of the saline solution was determined by measuring the output from the probes in solutions of constant salinity over a range of temperatures. The temperature coefficient was determined to be 1.8% ± 0.1% per degree centigrade, where an increase in temperature resulted in an increase in conductivity.

After use the probes were carefully washed with distilled water and then placed in bottles of distilled water to minimize the degradation of the platinization during storage prior to the next experiment.



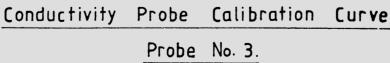


FIGURE 46.

APPENDIX 4

EVALUATION OF K AND
$$\psi$$

EVALUATION OF K

 K_{b} has been given in Equation (28) as:

$$K_{b} = \left\{ 8S_{1} \frac{g_{b}'}{g_{1}'} \left[\frac{(1+C_{v})F_{b}^{2}}{2} + \chi \right] \right\}^{1/3}$$
(28)

Experimental observations have shown that the shape of the broken wave may be well approximated by a half ellipse of height (H) and length (L). For an aspect ratio (H/L) of 0.3 as given in Section (2) it is a simple matter of geometry to show that S_1 (= A/H^2), where A is the sectional area is given by:

$$S_1 = \pi/1.2$$

 $\frac{s}{1}$

The virtual mass coefficient (C_v) is given by Robertson (1965) as a function of the aspect ratio (H/L) of the body. For the mean aspect ratio, as determined from experiments of 0.3, the value of the virtual mass coefficient is:

$$C_v \simeq 0.6$$

 χ , which allows for the shape of the wave profile and the density distribution therein when determining the elevation of the centroid was given in Equation (22) as:

126

$$\chi = \frac{\left[\int \int zd(g'A)\right]_{b}}{g_{b}'H_{b}A_{b}}$$
(22)

As noted on the previous page the wave shape may be approximated by a semi-ellipse. The form of the density distribution at breaking as shown in Figure (34) may be approximated by a quarter ellipse. χ therefore represents the normalised elevation of the centroid of a quarter ellipsoid, which is given by Tuma (1979) as:

x = 0.375

Experimental values of K_{b} are given in Table (3) in Section (6).

Evaluation of ψ

 ψ has been given by Equation (44) as:

$$\psi = \frac{1}{5(1+C_v)} \left[\frac{2S_o}{IF^2} + \frac{C_d}{S_1} \right]$$
(44)

The values of S_1 and C_v are the same as determined previously, that is:

 $S_1 = \pi/1.2$ $C_v \simeq 0.6$

<u>C</u>d

An expression for the drag coefficient (C_d) will be derived by assuming that the form of a broken internal wave and the head of a gravity current are similar. The drag coefficient (C_d) for a broken internal wave may then be approximated by the drag coefficient acting on the head of a gravity current. Consider the flow pattern sketched in Figure (47) where a gravity current with head height (H_G) , tail height (h_G) and density excess (Δ_G) propagates with celerity (c_G) along a horizontal bed. For steady flow the sum of the forces acting on the head parallel to the bed must be zero, that is:

$$EF = [F_{AA} - F_{BB}] - F_{D} = 0$$
 (60)

where ΣF = the sum of the forces acting on the head F_{AA} = the pressure force across Section AA F_{BB} = the pressure force across Section BB and F_{D} = the drag force acting on the gravity current head

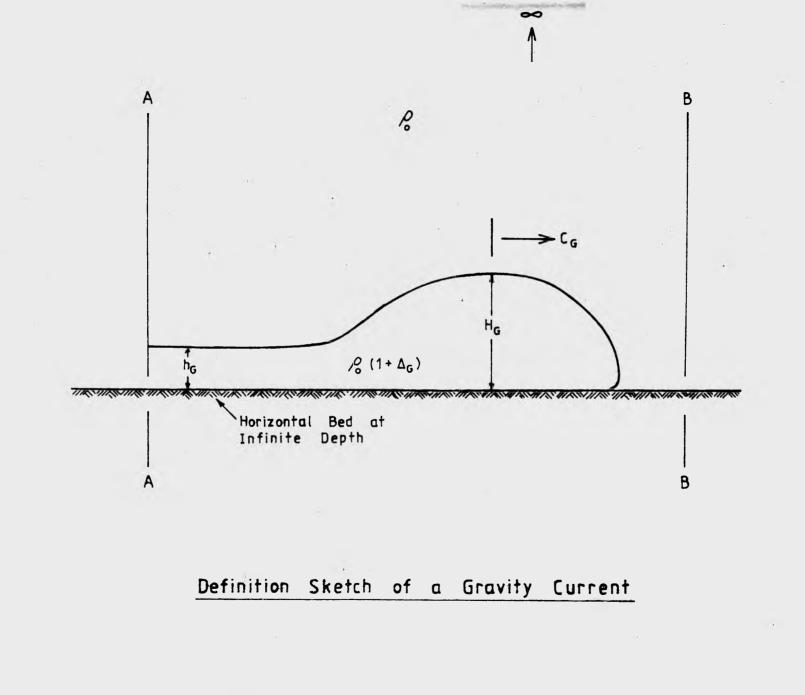
The differential force $[F_{AA} - F_{BB}]$ between AA and BB is given by:

$$F_{AA} - F_{BB} = \Delta_{G} \rho_{o} gh_{G}^{2}/2$$
(61)

and the drag force is given by:

F

$$D = C_d \rho_0 c_G^2 H_G/2$$



Substituting for $[F_{AA} - F_{BB}]$ and F_{D} from Equations (61) and (62) into Equation (60) and rearranging yields an expression for the drag coefficient (C_{d}) as:

(63)

$$C_{d} = \frac{h_{G}}{H_{G}} \cdot \frac{\Delta_{G}gh_{G}}{C_{G}^{2}}$$

The parameters in Equation (63) may be evaluated by using the results of studies undertaken by Benjamin (1968) and Wilkinson and Wood (1972). According to Benjamin, H_G is generally taken to be about twice h_G . Wilkinson and Wood give, for the range of F used in the experiments, a mean value for $c_G^2/\Delta_G gh_G$ of 1.2. Substituting these values into Equation (63) gives:

$$C_d \simeq 0.42$$

Experimental values of ψ for each of the experiments are given in Table (4) in Section (6).

APPENDIX 5

130

LIST OF SYMBOLS

A

А

A

Az

a

b

C_d

C,

·c

съ

°G

°,

D

d

d

du

e

ЕЪ

E,

=	The sectional area of a broken 2-dimensional wave
=	S ₁ H ²
=	The sectional area of a 2-dimensional wave at breaking
=	S ₁ H _b ²
=	Area beneath the normalised density curve as defined in
	Figure (34)
=	Area between the crest and trough density excess profiles
	as shown in Figure (30)
-	A dimensionless constant
=	A dimensionless constant
=	A drag coefficient
=	The virtual mass coefficient
=	M _v /ρA
=	Celerity of broken internal wave propagating upslope
= .	Wave celerity at breaking
=	Celerity of the head of a gravity current as defined in
	Figure (47)
=	Wave celerity in the constant depth section of the flume
=	Equivalent fluid depth
=	$d_u d_{\ell} / (d_u + d_{\ell})$
=	Depth of water
=	Depth of lower layer
=	Depth of upper layer
=	A dimensionless constant
=	Energy of a single wave at breaking
=	$E_{k} + E_{p}$
= .	Energy of a single wave in the constant depth section of
	the flume

$ = \rho g_1' H_1^{-2} \lambda_1/3 $ $ F_k = Kinetic energy of a single wave at breaking = \frac{1}{2} \rho A_b (1 + C_y) c_b^2 F_p = Potential energy of a single wave at breaking = \rho A_b g_b' z_b F = A Force F = A Froude number = c/(g'B)^{1/2} F_b = The Froude number at breaking = c_b/(g_b'H_b)^{1/2} g = Acceleration due to gravity g' = Effective gravitational acceleration = \Delta g F_b' = Ffective gravitational acceleration at breaking \Delta_b g F_t' = Effective gravitational acceleration in the constant depth section of the flume = \Delta_1 g H = Height of broken internal wave propagating upslope H_b = Wave height at breaking H_c = Height of the head of a gravity current as defined in Figure (47) H_1 = Wave height in the constant depth section of the flume H_o' = Unrefracted deepwater (surface) wave height + h_d = Depth of backflow upslope of wave + h_c = Depth of backflow upslope of wave + h_c = Depth of backflow upslope of wave + h_c = Ref_{g_1'} (1 + C_y)F_b^2 + x_1 Y_1 = Vave height in flume = Vave + K_b = \begin{cases} a_5 \frac{a_b'}{a_1'} \frac{(1 + C_y)F_b^2}{2} + x_1 \end{cases} \frac{1/3}{3} $			
$ F_k = Kinetic energy of a single wave at breaking = \frac{1}{2} \rho A_b (1 + C_v) c_b^2 F = Potential energy of a single wave at breaking= \rho A_b g_b' z_bF = A ForceF = A Force number= c/(g'H)^{1/2}F_b = The Froude number at breaking= c_b/(g_b'H_b)^{1/2}g = Acceleration due to gravityg' = Effective gravitational acceleration= \Delta gb_b' = Effective gravitational acceleration at breaking\Delta_b gb_b' = Effective gravitational acceleration in the constantdepth section of the flume= \Delta_1 gH = Height of broken internal wave propagating upslopeH_b = Wave height at breakingH_G = Height of the head of a gravity current as defined inFigure (47)H_1 = Wave height in the constant depth section of the flumeH_0' = Unrefracted deepwater (surface) wave heighth_d = Depth of backflow downslope of waveh_G = Depth of flow behind the head of a gravity current asdefined in Figure (47)h_i = Depth of backflow upslope of waveh_1 = Depth of backflow upslo$		=	ρg, ¹ H, ² λ, /8
$= \frac{1}{2} p A_b (1 + c_v) c_b^2$ $E_p = Potential energy of a single wave at breaking = p A_b B_b' z_b F = A Force F = A Froude number = c/(g'H)^{1/2} F_b = The Froude number at breaking = c_b/(g_b'H_b)^{1/2} g = Acceleration due to gravity g' = Effective gravitational acceleration = \Delta g B_b' = Effective gravitational acceleration at breaking \Delta_b g B_1' = Effective gravitational acceleration in the constant depth section of the flume = \Delta_1 g H = Height of broken internal wave propagating upslope H_b = Wave height at breaking H_G = Height of the head of a gravity current as defined in Figure (47) H_1 = Wave height in the constant depth section of the flume H_0' = Unrefracted deepwater (surface) wave height H_d = Depth of flow behind the head of a gravity current as defined in Figure (47) H_i = Depth of backflow downslope of wave$	E	=	
$ = \rho A_b g_b' z_b $ F = A Force F = A Froude number $ = c/(g'H)^{1/4}$ F = The Froude number at breaking $ = c_b/(g_b'H_b)^{1/2}$ g = Acceleration due to gravity g' = Effective gravitational acceleration $ = Ag$ g = Effective gravitational acceleration at breaking $ A_b g$ g = Effective gravitational acceleration in the constant depth section of the flume $ = A_1 g$ H = Height of broken internal wave propagating upslope H = Wave height at breaking H = Height of the head of a gravity current as defined in Figure (47) H = Unrefracted deepwater (surface) wave height h = Depth of flow behind the head of a gravity current as defined in Figure (47) h = Depth of backflow upslope of wave	ĸ	=	
$ = \rho A_b g_b' z_b $ F = A Force F = A Froude number $ = c/(g'H)^{1/4}$ F = The Froude number at breaking $ = c_b/(g_b'H_b)^{1/2}$ g = Acceleration due to gravity g' = Effective gravitational acceleration $ = Ag$ g = Effective gravitational acceleration at breaking $ A_b g$ g = Effective gravitational acceleration in the constant depth section of the flume $ = A_1 g$ H = Height of broken internal wave propagating upslope H = Wave height at breaking H = Height of the head of a gravity current as defined in Figure (47) H = Unrefracted deepwater (surface) wave height h = Depth of flow behind the head of a gravity current as defined in Figure (47) h = Depth of backflow upslope of wave	E	=	Potential energy of a single wave at breaking
$F = A Force$ $F = A Force$ $F = A Froude number$ $= c/(g'H)^{1/2}$ $F_{b} = The Froude number at breaking$ $= c_{b}/(g_{b}'H_{b})^{1/2}$ $g = Acceleration due to gravity$ $g' = Effective gravitational acceleration$ $= \Delta g$ $g_{b}' = Effective gravitational acceleration at breaking$ $\Delta_{b}g$ $g_{1}' = Effective gravitational acceleration in the constant depth section of the flume = \Delta_{1}g H = Height of broken internal wave propagating upslope H_{b} = Wave height at breaking H_{c} = Height of the head of a gravity current as defined in Figure (47) H_{1} = Wave height in the constant depth section of the flume H_{o}' = Unrefracted deepwater (surface) wave height H_{c} = Depth of flow behind the head of a gravity current as defined in Figure (47) H_{1} = Depth of backflow upslope of wave$	Р	=	
$= c/(g'H)^{1/2}$ $F_{b} = The Froude number at breaking$ $= c_{b}/(g_{b}'H_{b})^{1/2}$ $g = Acceleration due to gravity$ $g' = Effective gravitational acceleration$ $= \Delta g$ $g_{b}' = Effective gravitational acceleration at breaking$ $\Delta_{b}g$ $g_{1}' = Effective gravitational acceleration in the constant depth section of the flume$ $= \Delta_{1}g$ $H = Height of broken internal wave propagating upslope$ $H_{b} = Wave height at breaking$ $H_{c} = Height of the head of a gravity current as defined in Figure (47)$ $H_{1} = Wave height in the constant depth section of the flume$ $H_{o}' = Unrefracted deepwater (surface) wave height$ $h_{d} = Depth of backflow downslope of wave$ $h_{f} = Depth of backflow upslope of wave$	F	=	
$ F_b = The Froude number at breaking $	IF	=	A Froude number
$= c_b/(g_b'H_b)^{1/2}$ $g = Acceleration due to gravity$ $g' = Effective gravitational acceleration$ $= \Delta g$ $g_b' = Effective gravitational acceleration at breaking \Delta_b g g_1' = Effective gravitational acceleration in the constant depth section of the flume = \Delta_1 g H = Height of broken internal wave propagating upslope H_b = Wave height at breaking H_G = Height of the head of a gravity current as defined in Figure (47) H_1 = Wave height in the constant depth section of the flume H_0' = Unrefracted deepwater (surface) wave height h_d = Depth of backflow downslope of wave h_G = Depth of flow behind the head of a gravity current as defined in Figure (47)$		=	c/(g'H) ^{1/2}
$= c_b/(g_b'H_b)^{1/2}$ $g = Acceleration due to gravity$ $g' = Effective gravitational acceleration$ $= \Delta g$ $g_b' = Effective gravitational acceleration at breaking \Delta_b g g_1' = Effective gravitational acceleration in the constant depth section of the flume = \Delta_1 g H = Height of broken internal wave propagating upslope H_b = Wave height at breaking H_G = Height of the head of a gravity current as defined in Figure (47) H_1 = Wave height in the constant depth section of the flume H_0' = Unrefracted deepwater (surface) wave height h_d = Depth of backflow downslope of wave h_G = Depth of flow behind the head of a gravity current as defined in Figure (47)$	Fb	=	The Froude number at breaking
g' = Effective gravitational acceleration = Δ_g B_b' = Effective gravitational acceleration at breaking $\Delta_b g$ B_1' = Effective gravitational acceleration in the constant depth section of the flume = $\Delta_1 g$ H = Height of broken internal wave propagating upslope H _b = Wave height at breaking H _G = Height of the head of a gravity current as defined in Figure (47) H ₁ = Wave height in the constant depth section of the flume H _o ' = Unrefracted deepwater (surface) wave height h _d = Depth of backflow downslope of wave h _g = Depth of flow behind the head of a gravity current as defined in Figure (47) h ₁ = Depth of backflow upslope of wave	-	=	$c_{b}^{\prime}/(g_{b}^{\prime}H_{b}^{\prime})^{1/2}$
 Ag Effective gravitational acceleration at breaking	g	=	Acceleration due to gravity
$g_b' = Effective gravitational acceleration at breaking \Delta_b gg_1' = Effective gravitational acceleration in the constant depth section of the flume = \Delta_1 gH = Height of broken internal wave propagating upslopeH_b = Wave height at breakingH_C = Height of the head of a gravity current as defined in Figure (47) H_1 = Wave height in the constant depth section of the flumeH_o' = Unrefracted deepwater (surface) wave heighth_d = Depth of backflow downslope of waveh_G = Depth of flow behind the head of a gravity current as defined in Figure (47) h_i = Depth of backflow upslope of wave$	g'	=	Effective gravitational acceleration
 b b b a b a b a b a b c a b b c c d d		=	Δg
 g₁' = Effective gravitational acceleration in the constant depth section of the flume a₁g H = Height of broken internal wave propagating upslope H_b = Wave height at breaking H_G = Height of the head of a gravity current as defined in Figure (47) H₁ = Wave height in the constant depth section of the flume H_o' = Unrefracted deepwater (surface) wave height h_d = Depth of backflow downslope of wave h_G = Depth of flow behind the head of a gravity current as defined in Figure (47) 	g _b '	=	Effective gravitational acceleration at breaking
$depth section of the flume$ $= \Delta_1 g$ $H = Height of broken internal wave propagating upslope$ $H_b = Wave height at breaking$ $H_G = Height of the head of a gravity current as defined in Figure (47)$ $H_1 = Wave height in the constant depth section of the flume$ $H_0' = Unrefracted deepwater (surface) wave height$ $h_d = Depth of backflow downslope of wave$ $h_G = Depth of flow behind the head of a gravity current as defined in Figure (47)$ $h_i = Depth of backflow upslope of wave$			Δ _b g
 = Δ₁g H = Height of broken internal wave propagating upslope H_b = Wave height at breaking H_G = Height of the head of a gravity current as defined in Figure (47) H₁ = Wave height in the constant depth section of the flume H_o' = Unrefracted deepwater (surface) wave height h_d = Depth of backflow downslope of wave h_G = Depth of flow behind the head of a gravity current as defined in Figure (47) h_i = Depth of backflow upslope of wave 	gʻ.	=	Effective gravitational acceleration in the constant
 H = Height of broken internal wave propagating upslope H_b = Wave height at breaking H_G = Height of the head of a gravity current as defined in Figure (47) H₁ = Wave height in the constant depth section of the flume H₀' = Unrefracted deepwater (surface) wave height h_d = Depth of backflow downslope of wave h_G = Depth of flow behind the head of a gravity current as defined in Figure (47) h_i = Depth of backflow upslope of wave 			depth section of the flume
H _b = Wave height at breaking H _G = Height of the head of a gravity current as defined in Figure (47) H ₁ = Wave height in the constant depth section of the flume H ₀ ' = Unrefracted deepwater (surface) wave height h _d = Depth of backflow downslope of wave h _G = Depth of flow behind the head of a gravity current as defined in Figure (47) h _i = Depth of backflow upslope of wave		=	Δ _l g
H _G = Height of the head of a gravity current as defined in Figure (47) H ₁ = Wave height in the constant depth section of the flume H ₀ ' = Unrefracted deepwater (surface) wave height h _d = Depth of backflow downslope of wave h _g = Depth of flow behind the head of a gravity current as defined in Figure (47) h _i = Depth of backflow upslope of wave	Н	=	Height of broken internal wave propagating upslope
<pre>Figure (47) H₁ = Wave height in the constant depth section of the flume H₀' = Unrefracted deepwater (surface) wave height h_d = Depth of backflow downslope of wave h_G = Depth of flow behind the head of a gravity current as defined in Figure (47) h_i = Depth of backflow upslope of wave</pre>	Н _ь	=	Wave height at breaking
H ₁ = Wave height in the constant depth section of the flume H ₀ ' = Unrefracted deepwater (surface) wave height h _d = Depth of backflow downslope of wave h _G = Depth of flow behind the head of a gravity current as defined in Figure (47) h _i = Depth of backflow upslope of wave	н _G	=	Height of the head of a gravity current as defined in
<pre>H'' = Unrefracted deepwater (surface) wave height h'' = Depth of backflow downslope of wave h'' = Depth of flow behind the head of a gravity current as</pre>			Figure (47)
<pre>h_d = Depth of backflow downslope of wave h_G = Depth of flow behind the head of a gravity current as</pre>	Н	=	Wave height in the constant depth section of the flume
<pre>d h_G = Depth of flow behind the head of a gravity current as defined in Figure (47) h_i = Depth of backflow upslope of wave</pre>	н ′	=	Unrefracted deepwater (surface) wave height
defined in Figure (47) h = Depth of backflow upslope of wave	h d	=	Depth of backflow downslope of wave
h = Depth of backflow upslope of wave	h _G	=	Depth of flow behind the head of a gravity current as
1 .			defined in Figure (47)
$K_{b} = \left\{ 8S_{1} \frac{g_{b}}{g_{1}} \left[\frac{(1+C_{v})F_{b}^{2}}{2} + \chi \right] \right\}^{1/3}$	h _i	=	
	КЪ	=	$\left\{ 8S_{1} \frac{g_{b}}{g_{1}'} \left[\frac{(1+C_{v})F_{b}^{2}}{2} + \chi \right] \right\}^{1/3}$

Wave number

 $2\pi/\lambda_{o}$

k

T.

LR

M

N

q_d

IR

Ri

S

S,

T

Length of broken internal wave propagating upslope The model to prototype length scale

The virtual mass of the broken wave form

Brunt-Vaisala frequency

 $\left(\frac{-g}{\rho} \quad \frac{\partial \rho}{\partial z}\right)^{1/2}$

Rate of backflow downslope of wave

Rate of backflow upslope of wave

A Reynolds number

cH/v

A Richardson Number

 $\frac{\left[\frac{\rho_{\ell}-\rho_{u}}{\overline{\rho}}\right]gd_{u}/c^{2}}{\overline{\rho}}$

Bedslope

sin (B)

A dimensionless shape factor

A/H²

A shape factor for the backflow

$$\frac{h_i}{q_i^2} \int_{z=0}^{h_i} [(u_i(z))]^2 dz$$

Wave period

Time

The model to prototype time scale

A velocity approximately parallel to the bed

A distance measured along the sloping shelf from the breakpoint

Chainage measured up the sloping shelf from the intersection of the horizontal and sloping beds The chainage at which the wave breaks z A vertical distance The elevation of the centroid of the breaking wave mass z, above the mean level of the quiescent halocline χH_b The 20% normalised density excess level as defined in ^z0.2 = Figure (31) The 80% normalised density excess level as defined in z_{0.8} Figure (31) β Angle of the bed to the horizontal = Г A dimensionless constant = Ĺ Mean density excess within the broken wave propagating upslope $\frac{1}{H} \int_{-\infty}^{H} \Delta(z) dz$ $\Delta(z) =$ The vertical distribution of density excess within the broken wave Ь Mean density excess within the wave at breaking $\frac{1}{H_{b}}\int_{z=0}^{H_{b}}\Delta_{b}(z).dz$

 $\Delta_{b}(z) =$ The vertical distribution of density excess within the wave at breaking

 Δ_d = Density excess in backflow downslope of wave

- Δ_{G} = Density excess within a gravity current as defined in Figure (47)
- Δ_i = Density excess in backflow upslope of wave
- Δ = Density excess within the wave in the constant depth section of the flume

 $(\rho_{\chi} - \rho_{\mu})/\overline{\rho}$

θ = Angle of wave propagation to the horizontal in a continuously stratified fluid $= \cos^{-1}(\omega/N)$

 $\lambda_0 = Deepwater wavelength$

 λ_1 = Wavelength in the constant depth section of the flume

= Kinematic viscosity

 ρ = Density

 ρ_{k} = Density of a constant depth lower layer

 ρ_{o} = Density of ambient fluid

 ρ_u = Density of a constant depth upper layer

Ā

X

\$2

ω

=

=

=

ν

 $= (\rho_{\rm u} + \rho_{\rm g})/2$

 $\frac{\left[\int \int zd(g'A)\right]_{b}}{g'A}$ $\frac{g'A}{g_{b}'H_{b}A_{b}}$ $\frac{1}{5(1+C_{v})}\left[\frac{2S_{o}}{\mathbb{F}} + \frac{C_{d}}{S_{1}}\right]$

= A function of d_u/d_l

Wave frequency

APPENDIX 6

135

APPLICATION TO PROTOTYPE

Scaling

In this section are described the method for scaling model parameters to prototype conditions.

Long internal waves are basically a gravitational-inertial phenomena and should therefore be scaled using the bulk Richardson number and similarity of boundary geometry in the model and the prototype. The bulk Richardson number (Ri) in this application is given by:

$$Ri = \left[\frac{\rho_{\mu} - \rho_{u}}{\overline{\sigma}}\right] g d_{u} / c^{2}$$
(64)

where ρ_u = density of the upper layer ρ_{χ} = density of the lower layer $\overline{\rho}$ = $(\rho_u + \rho_{\chi})/2$ g = acceleration due to gravity d_u = the depth of the interface c = the internal wave celerity

However, the celerity of a long internal wave was given by Equation (59) as:

$$c = \left[\frac{\rho_{\chi} - \rho_{u}}{\overline{\rho}} g d_{u}\right]^{1/2} \sqrt{\left[\frac{d}{d_{\chi}}\right]}$$
(59)

Provided $(\rho_{\ell} - \rho_{u})/\bar{\rho} \ll 1$ it follows that the selection of $(\rho_{\ell} - \rho_{u})/\bar{\rho}$ is arbitrary and the Richardson number criteria will always be satisfied.

On a continental shelf, in "shallow" water, Equation (59) becomes:

$$c = \left[\frac{\rho_{\chi} - \rho_{u}}{\overline{\rho}} g \frac{d_{u} d_{\ell}}{d_{u} + d_{\chi}}\right]^{1/2}$$
(65)

The time scale (t_R) is determined by Equation (64) and is given by:

$$t_{R} = \left[\frac{\overline{\rho}}{\rho_{\ell} - \rho_{u}}\right]_{R}^{1/2} L_{R}^{1/2}$$
(66)

where $L_R =$ the model to prototype length scale $(\overline{\rho}/(\rho_{\ell} - \rho_u))_R =$ the scale of density differences.

The length scale in the model was approximately 4×10^{-3} while $(\overline{p}/(\rho - \rho_u))_R$ was approximately 10^{-2} yielding a time scale of 6×10^{-3} . Thus the wave periods of 6 to 19 seconds used in the laboratory experiments corresponded to prototype waves with periods of approximately 15 minutes to 1 hour.